Estudios Geológicos
enero-junio 2023, 79(1), e148
ISSN-L: 0367-0449
https://doi.org/10.3989/egeol.44694.617

Structural and mineral mapping using multispectral images in the Central High Atlas of Morocco

Cartografía estructural y mineral mediante imagen multiespectral en el Alto Atlas Central de Marruecos

Hayat Ait Inoh[a]*, Abdelatif Rajji[b], Mounir Eddardouri[a], Mohamed Tayebi[a]

[a] Research Team of Geosciences, Faculty of Science, Ibn Tofail University, Kenitra, Morocco. ORCID ID: https://orcid.org/0000-0002-8418-6791, https://orcid.org/0000-0001-7253-3445, https://orcid.org/0000-0001-7999-4260
[b] Research Team of Biotechnology, Valorization of Phytojenetic Ressources, Faculty of Sciences, Sultun Molay Sliman University, Beni Mellal, Morocco. ORCID ID: https://orcid.org/0000-0002-5323-9723
* Corresponding autor: Hayat.aitinoh@gmail.com

ABSTRACT

The Central High Atlas is one of the geological structures that belong to the Moroccan Atlas massif. It presents a great geological diversity and many structural and facies features. It is controlled by main faults of N70 to E-W direction that are visible at different scales and is rich in numerous mineralized veins. This area was the subject of the present work, in which we simulated the images of Landsat 8 OLI, Sentinel 2, and Aster sensors to map the hydrothermal alteration minerals associated with a lithostructural mapping that can provide more information on the mineralization of this study area. We highlight different approaches to remote sensing, considering first the methods of extraction of lineaments from the infrared-band of the Landsat 8 OLI image and from the GDEM ASTER to highlight the geological features of the study area. To obtain a good discrimination of the lithological units, Principal Component Analysis and Optimal Index Factor were applied to create colored composites with a better visual interpretation in order to generate a good lithological mapping, and finally, many band ratios are proposed for ASTER, Landsat 8 OLI and Sentinel 2 to derive several maps corresponding to the hydrothermal alteration zones that are compared to the geological map of the studied site, presenting a favorable correlation between them. The analysis of the results of the obtained maps allowed us to identify the main structural directions encompassing the NE-SW to E-W, NNE-SWSW and ENE-WSW families and also allowed us to highlight two potential zones of mineralization; one located to the south of Demnate at the western end of the Central High Atlas and the other in the middle part of the Central High Atlas. The superposition of the alteration maps and the fracturing map shows that the zones that are favorable for mineralization deposits are affected by faults in a generally NE-SW direction.

Keywords: Central High Atlas; Remote sensing; Landasat 8 OLI; Aster; Sentinel 2; Lithostructural Maps; Hydrothermal Alteration Mineral Mapping.

Recibido el 01 de mayo de 2022; Aceptado el 13 de diciembre de 2022; Publicado online el 31 de enero de 2023

Citation / Cómo citar este artículo: Ait Inoh, H. et al. (2022) Structural and mineral mapping using multispectral images in the Central High Atlas of Morocco. Estudios Geológicos 79(1): e148. https://doi.org/10.3989/egeol.44694.617

RESUMEN

El Alto Atlas Central es una de las estructuras geológicas que pertenecen al Macizo del Atlas marroquí. Presenta una gran diversidad geológica y muchas características estructurales y de facies. Está controlada por fallas principales de dirección N70 a E-O, visibles a diferentes escalas y ricas en numerosas vetas mineralizadas. Esta zona ha sido objeto del presente trabajo, en el que hemos simulado las imágenes de los sensores Landsat 8 OLI, Sentinel 2 y Aster para cartografiar los minerales de alteración hidrotermal asociados a una cartografía litoestructural que puede aportar más información sobre la mineralización de esta zona de estudio. En este punto destacamos los diferentes enfoques de teledetección adoptados, citando en primer lugar los métodos de extracción de lineamientos a partir de la banda infrarroja de la imagen Landsat 8 OLI y del GDEM ASTER para destacar la fracción geológica del área de estudio. Para obtener una buena discriminación de las unidades litológicas se realizó un Análisis de Componentes Principales y se aplicó el Factor de Índice Óptimo para crear composiciones de color con mejor interpretación visual para tener una buena cartografía litológica, y finalmente, se proponen muchas relaciones de bandas para ASTER, Landsat 8 OLI y Sentinel 2 para derivar varios mapas correspondientes a las zonas de alteración hidrotermal que se comparan con el mapa geológico del lugar estudiado, que presenta una correlación favorable entre ellos. El análisis de los resultados de los mapas obtenidos permitió identificar las grandes direcciones estructurales materializadas por las familias NE-SW a E-W, NNE-SWSW y ENE-WSW y también permitió destacar dos zonas potenciales de mineralización: una situada al sur de Demnate en el extremo occidental del Alto Atlas Central y la otra en la parte central del Alto Atlas Central. La superposición de los mapas de alteración y del mapa de fracturación muestra que las zonas que pueden ser favorables para los depósitos de mineralización están afectadas por fallas en dirección generalmente NE-SW.

Palabras clave: Alto Atlas Central; Teledetección; Landasat 8 OLI; Aster; Sentinel 2; Mapas Litoestructurales; Cartografía Mineral de Alteración Hidrotermal.

Introduction

Due to the development of remote sensing technologies, satellite data has become capable of improving the accuracy of geological maps in a robust, fast, and simple manner especially in areas of difficult access, as opposed to conventional methods, which are costly, risky, and time-consuming. Hydrothermal alteration mineral exploration mapping by spectral remote sensing allows for the discrimination and identification of new areas of hydrothermal alteration minerals (Amer *et al.*, 2012) composed of at least one mineral with a spectral feature (Azizi *et al.*, 2010). Several studies have proven the reliability of multispectral and hyperspectral data processing for the identification of hydrothermal alteration zones (Rowan *et al.*, 2003; El Atillah *et al.*, 2018; Bolouki *et al.*, 2020).

This study is a contribution to the geological mapping of the Central High Atlas, which is marked by the presence of intense fracturing accompanied by several mining occurrences, generated during the geological history of the Atlas Mountains. The main objective of this work is the use of satellite images from Landsat 8 OLI, Aster, and Sentinel 2 in an attempt to geologically map the Central High Atlas. The choice of digital mapping is part of the prospect of exploiting all the digital information available for the compilation of cartographic data in this area.

It is in this sense that we propose this approach, which focuses first on structural mapping from Landsat 8 OLI and ASTER GDEM images that make a considerable contribution to the establishment of structural maps (Varas, 2006; Alshayef and Javed, 2018; Chabane *et al.*, 2019; Ait Inoh *et al.*, 2022) to highlight some major structures and accidents barely visible on the ground by applying directional filters.

The processing of Landsat OLI, Sentinel 2, and Aster satellite images also contributes, in an efficient way, to lithological and mineralogical mapping by applying image processing techniques such as band ratio (BR) (Kalinowski and Oliver, 2004; Gozzard, 2006; Van der Meer *et al.*, 2014), Optimum Index Factor calculation (Berraki *et al.*, 2012; El Atillah *et al.*, 2018) and Principal Component Analysis (Tangestani *et al*., 2008; Amer *et al*., 2010) to detect areas of spectral mineral anomalies associated with the presence of hydrothermal or supergene alteration in the study area.

The resulting maps were interpreted and validated against the geological maps to provide a summary document of the lineaments and map distribution of alteration zones in the Central High Atlas, to be used as a guide for mineral exploration.

Description of the study area

Geology

The Calcareous High Atlas (Mattauer *et al*., 1977) or Central High Atlas (Michard, 1976) is limited by the Marrakech-Ouarzazate transverse line in the west and the valley of the Oued Ziz in the east. The source rock is rarely apparent and there are scarcely any outcrops of the Mesozoic covering known as the "folded Atlantic cover", the sediments of which form characteristic series. The red terrigenous deposits of the Permo-Triassic overlie the White carbonates of the Lower Jurassic (Ait Addi & Chafiki, 2013; Igmoullan *et al.,* 2001; Teixell *et al.,* 2017). In the Middle and Upper Jurassic, red terrigenous deposits are again found, this time strongly thickened (Ettaki *et al*., 2000; Haddoumi *et al.,* 2002; Chacrone & Hamoumi, 2005). The rare Cretaceous and Tertiary outcrops are often eroded in the center of the range and are preserved on the edges of the range (Michard *et al.,* 2011). In addition, magmatic rocks also outcrop here, including Triassic and Liassic basalts, as well as alkaline gabbros of Jurassic and Cretaceous ages. The latter is evidence of thinning of the continental crust by distension (Hailwood & Mitchell, 1971).

The uplift of the High Atlas is the result of a structural inversion from the Cretaceous to the Cenozoic, during which the post-Hercynian cover was folded and peeled off onto the detrital Triassic. Because of these deformations, the High Atlas is crossed by broad, flat-bottomed synclines filled by thick Jurassic and Cretaceous series, which are often heavily eroded. In contrast, the anticlines are sharp, narrow, upright, abrupt and often overlapping at their edges. They are a network of folds with an N 80°E axis, which are mostly echeloned (Jacobshagen *et al.*, 1986). These anticlines are mainly composed of thick Lower Lias limestones with local intrusions of Jurassic-Cretaceous magmatic rocks (*Essaifi & Zayane*, 2018). The High Atlas ejective style (Stets & Wurster, 1982; Jacobshagen *et al.*, 1988; Giese & Jacobshagen, 1992; Piqué *et al.*, 1993, Laville *et al.*, 2004) is responsible for a characteristic fan-shaped thrust with a northern vergence on the northern edge and a southern vergence on the southern edge. Depending on the author, the shortening appears to be either modest (10-15%) (Brede *et al.*, 1992) or strong (Brunet & Cloetingh, 2003).

Structures in the High Central Atlas Mountains

The Central High Atlas is an intracontinental structured mountain range as a succession of broad, flat-bottomed synclinal megastructures and sharp, narrow anticlinal megastructures. The synclines are sometimes lozenge-shaped and generally, show marl and limestone terrains of the Dogger superimposed in places by the red detrital series of the Bathonian (Haddoumi *et al.*, 2010):

-Callovian to Lower Cretaceous (Laville *et al.,* 1991; Fadile, 1987; Ibouh, 1995). The anticlines are mainly N70 to E-W in direction and sometimes with "S" or "Z" shaped vibrations (Ibouh *et al.*, 2001). The anticlinal structures are in places unhinged with a core occupied by a mega-breccia with elements of different natures such as Triassic, and/or Jurassic basaltic flows, Jurassic limestone flakes and Triassic pink clays.

Mineralization

At the scale of the Central High Atlas, the works of (Ibouh *et al.,* 2011; Mouguina, 1992, 2004; Mouguina *et al.*, 1999) have allowed the inventory of metallogenic periods, namely (Figure 1):

- A period related to the Liassic with economically unimportant Zn-Pb expressed as syngenetic mineralization hosted in massive Carixian-Domerian limestones. The mineral paragenesis consists of sphalerite and galena. This metallogenic event could be linked to the Triassic-Liassic thermogenic event, linked to the opening of the Central Atlantic.
- A period related to the Dogger, of greater economic importance, linked to the geodynamic evolution of the magmatic rifts of the Central High Atlas, during which two main mineralizing phases can be distinguished; the first phase is characterized by disseminated mineralization in Ni-Cu type gabbros, which is located at the contact of the Triassic facies. The mineral paragenesis is formed by pyrrhotite, chalcopyrite and pentlandite. The main gangue mineral is hornblende. The Ni-Cu minerali-

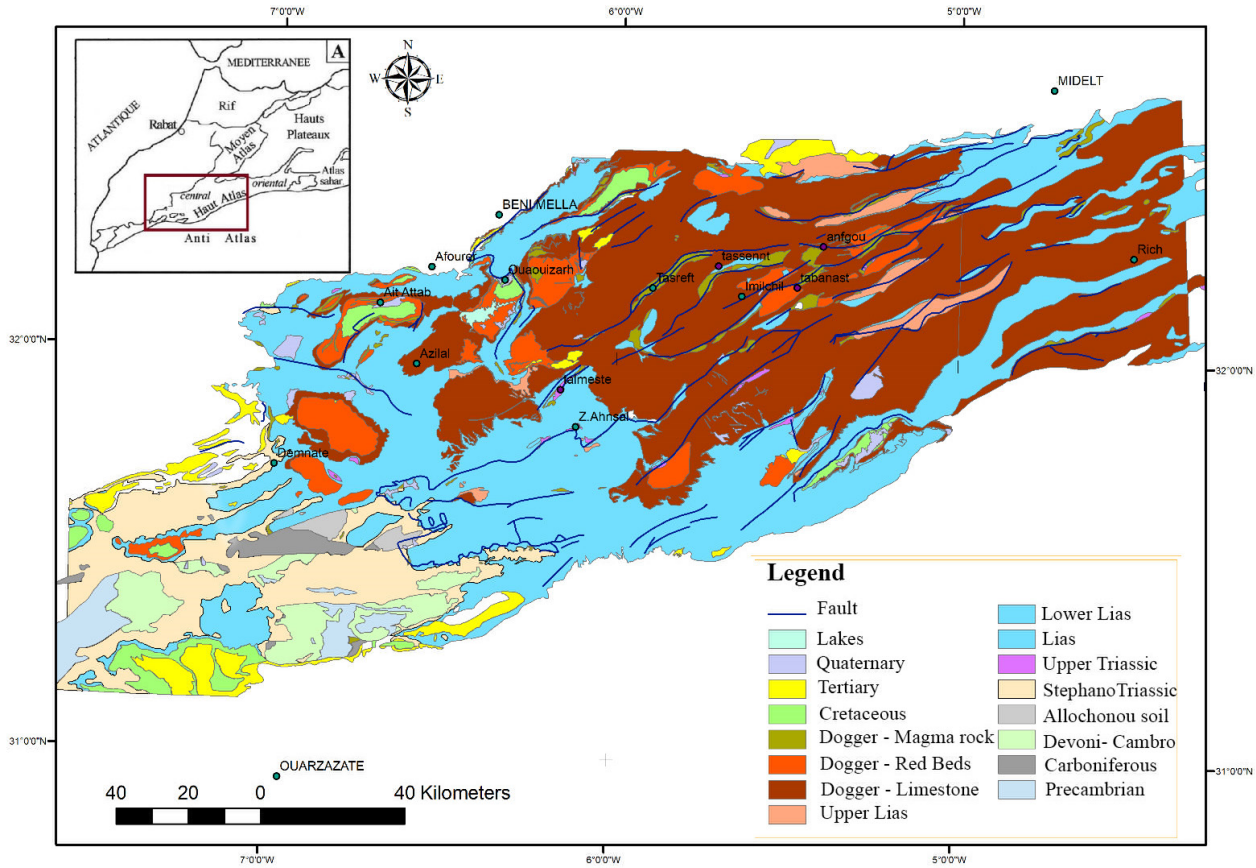

Figure 1.— Position of the deposits described on the 1/10000 geological map of the Central High Atlas (modified).

zation is said to be generated at temperatures ranging from 500 to 800°C and pressures of 3 to 6 Kbar. It results from a mixture of metals from late pneumatolytic fluids-fractional crystallization of gabbroic magmas and sulfur probably from Triassic evaporites. The second phase exists in the gabbros and the carbonate cover. In the gabbros, the Zn-Pb mineralization is disseminated and is linked to hydrothermal metamorphism of the greenschist type, guided by N-S direction fractures, oblique to the contacts with the Triassic. The mineralisation is sphalerite, rich galena and pyrite in a serpentine, talc, rich actinote and vermiculite gangue. Mineralogical data show that the mineralizing fluids that give rise to the mineral paragenesis of the second phase are thought to have formed at temperatures ranging from 150 to 300°C with depression of up to 2Kbars.

At the level of the carbonate cover, the second mineralizing period is translated in the massive Carixian-Domerian limestones of the Tazoult-Wawrirout deposit, by epigenetic mineralization with Zn, Pb, Cu of probably Aalenian age. This mineralization is emplaced in veins and mega-slits associated with the dextral transtensional play of E-W to N120 faults. The mineral paragenesis is sphalerite, galena±chalcopyrite± gersdorffite-arsenopyrite-enargite. The mineralized bodies should be formed as a result of a mixture of metals probably leached from the gabbros, as evidenced by the presence of gersdorffite and sulfur of Triassic or magmatic origin.

Data and Methodology

The mapping of linear structures and hydrothermal alteration minerals required the consideration

of remote sensing data and cartographic data that constitute several geological maps and structural schemes of the Central High Atlas at different scales. The remote sensing data used come from three types of sensors: Aster, Landsat, and Sentinel 2, which were acquired during the dry season using the Universal Transverse Mercator (UTM) projection and the WGS 84 world geodetic system (Table 1). These sensors represent Landsat 8 OLI images, which record data in nine VNIR and SWIR spectral bands (0.43-2. 29µm) with a spatial resolution of 30 m in addition to a panchromatic band at 15 m, the multispectral Sentinel 2 A images characterized by considerable spectral richness, which have 13 spectral bands spanning from visible and near-infrared to shortwave infrared (Drusch *et al.*, 2012) and ASTER (Advanced Spaceborne Thermal Emission and Reflection Radiometer) images with 14 spectral bands including 3 VNIR (visible and near-infrared), 6 SWIR (shortwave infrared) and 5 TIR (thermal infrared) which have been widely used in mineralogical and geological research (Rowan *et al.* 2003; Gabr *et al.*, 2010; Pour & Hashim, 2014).

The methodology adopted to achieve the objectives of this project is summarised in two parts (Figure 2); the first part is reserved for lineament map-

Table 1.— Spectral bands of used data in this study.

Landsat 8 OLI			Aster			Sentinel 2		
Band	Wavelenght	Résolution	Band	Wavelenght	Résolution	Band	Wavelenght	Résolution
1	0,43-0,45	30m	1	0. 52-0. 60	15m	1	0. 44	60m
2	0,45-0,51	30m	2	0. 63-0. 69	15m	2	0. 49	10m
3	0,53-0,59	30m	3N	0. 78-0. 86	15m	3	0. 56	10m
4	0,63-0,67	30m	3B	0. 78-0. 86	15m	4	0. 66	10m
5	0,85-0,87	30m	4	1. 60-1. 70	30m	5	0. 70	20m
6	1,56-1,65	30m	5	2. 15-2. 18	30m	6	0. 74	20m
7	2,10-2,29	30m	6	2. 18-2. 22	30m	7	0. 78	10m
8	0,50-0,67	15m	7	2. 23-2. 28	30m	8	0. 84	20m
9	1,36-1,38	30m	8	2. 29-2. 36	30m	8A	0. 86	60m
			9	2. 36-2. 43	30m	9	0. 94	60m
			10	8. 12-8. 47	90 m	10	1. 37	20m
			11	8. 47-8. 82	90 m	11	1. 61	20m
			12	8. 92-9. 27	90 m	12	2. 19	20m
			13	10.25-10.95	90 m			
			14	10.95-11. 65	90 m			

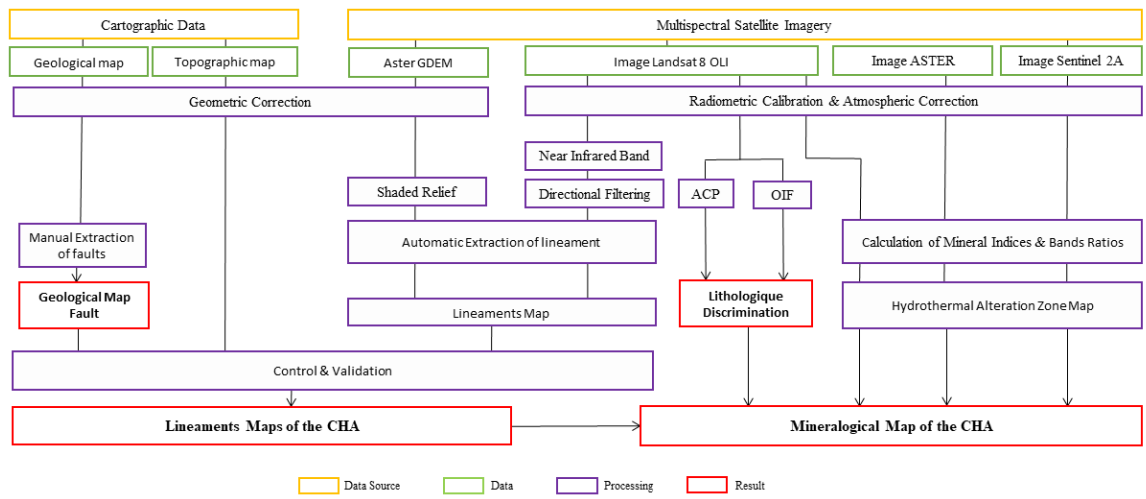

Figure 2.— A flow chart of the methodology adopted

Table 2.— The main metadata of Landsat OLI images used (http://Glovis.usgs.gov).

Metadata	Scene 1	Scene 2	Scene 3	Scene 4
Landsat Scene Identifier	LC820003720 17298LGN00	LC820003820 17298LGN00	LC820003820 17184LGN00	LC82010382017 209LGN00
Sensor	Landsat 8 OLI			
Acquisition date	07/11/2017	07/11/2017	15/07/2017	30/06/2017
Output Format	GEOTIFF			
Datum	WGS84			
UTM Zone	29		30	

Table 3.— The Sentinel 2 image metadata used in this work (http://Glovis.usgs.gov).

Metadata	Scene 1	Scene 2	Scene 3	Scene 4	Scene 5	Scene 6	Scene 7
Landsat Scene Identifier	L1C_T30S UB_A0055 54_201203 30T110002	L1C_T30S UB_A0055 54_201203 30T110150	L1C_T30S UB_A0055 54_201203 30T110002	L1C_T30S UB_A0055 54_2012044 0T110060	L1C_T30S UB_A0055 54_2012035 0T110800	L1C_T30S UB_A0055 54_2012033 0T140003	L1C_T30S UB_A0055 54_2012063 0T110001
Sensor	Sentinel 2						
Acquisition date	30/08/2017	15/11/2017	15/07/2017	30/06/2017	30/06/2017	30/03/2017	30/07/2017
Output Format	JPEG 2000						
Datum	WGS 84						
UTM Zone	30				29		

ping from Landsat 8 OLI and DEM imagery and the second part is based on the processing of Landsat 8 OLI, Aster and Sentinel 2 satellite imagery for the realization of different maps of mineralization and lithology. The pre-processing procedures are first the radiometric and atmospheric corrections applied to the satellite data to obtain corrected images, then the total coverage of the HAC required 4 scenes of the Landsat 8 OLI images (Table 2) and 7 scenes for the Sentinel 2 image (Table 3) and several Aster scenes which required a mosaic of the different scenes and then the extraction of the study area and finally, the geological maps were geo-referenced in a GIS environment to identify and analyze the different lineaments.

Extraction of lineaments under Landsat 8 OLI image and DEM

Lineament mapping aims to determine the linear structures corresponding to lithological or structural discontinuities and is achieved through the automatic extraction of linear structures from images processed by two different methods

The first method consists of the application of directional filters on the Landsat 8 OLI image (Figure 3), to enhance linear features in the image or features with a certain orientation in the image, such as in the case of faults in geology. For better visualization of the lineaments and taking into account the extent of the study area, the choice was made to apply the different sizes of matrix filters (3*3) and (7*7 matrix from Kouame, 1999; Youan *et al.*, 2008) of the Haralick 1984 filter (Fossati *et al.*, 1992; Rokos *et al.*,2000), which was applied to Near-infrared band of the Landsat 8 OLI image to enhance the lineaments in the N-S, NNE-SW, E-W and NNW-SSE directions.

The second method used to determine the lineaments is the shading map analysis (Muhammad & Awdal, 2012; Alhirmizy, 2015; Ait Inoh *et al.*, 2022) extracted from ASTER (Advanced Spaceborne Thermal Emission and Reflection Radiome-

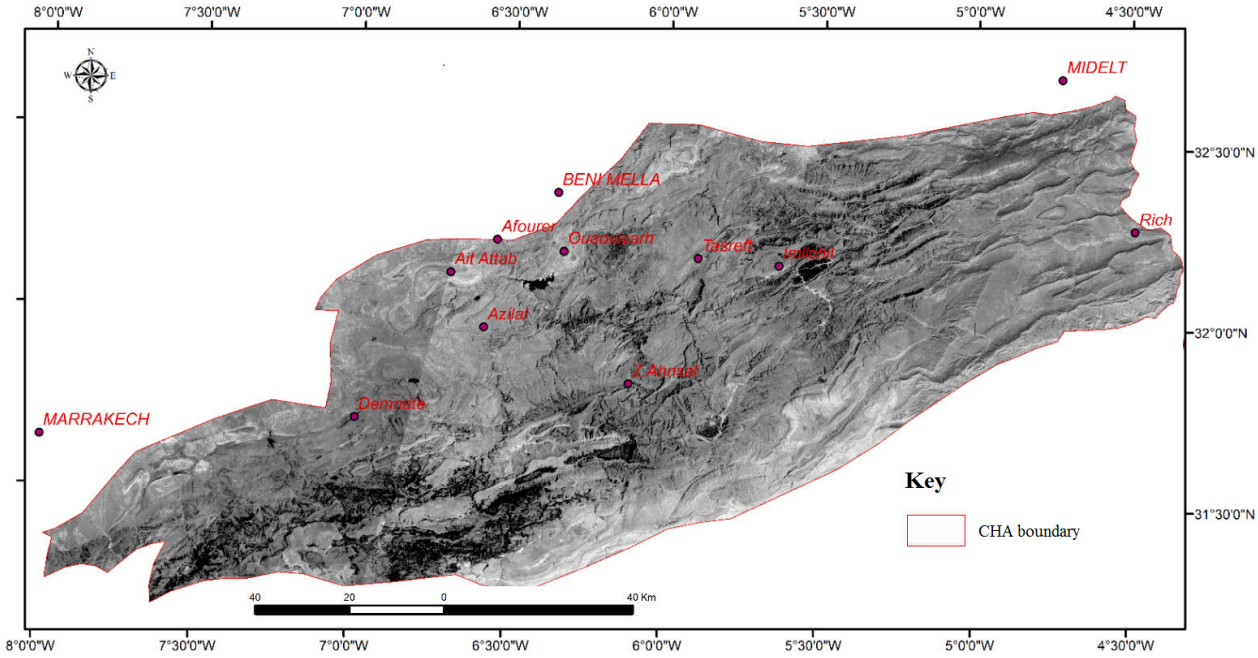

Figure 3.— Near-infrared Band of the Landsat OLI 8 image in greyscale.

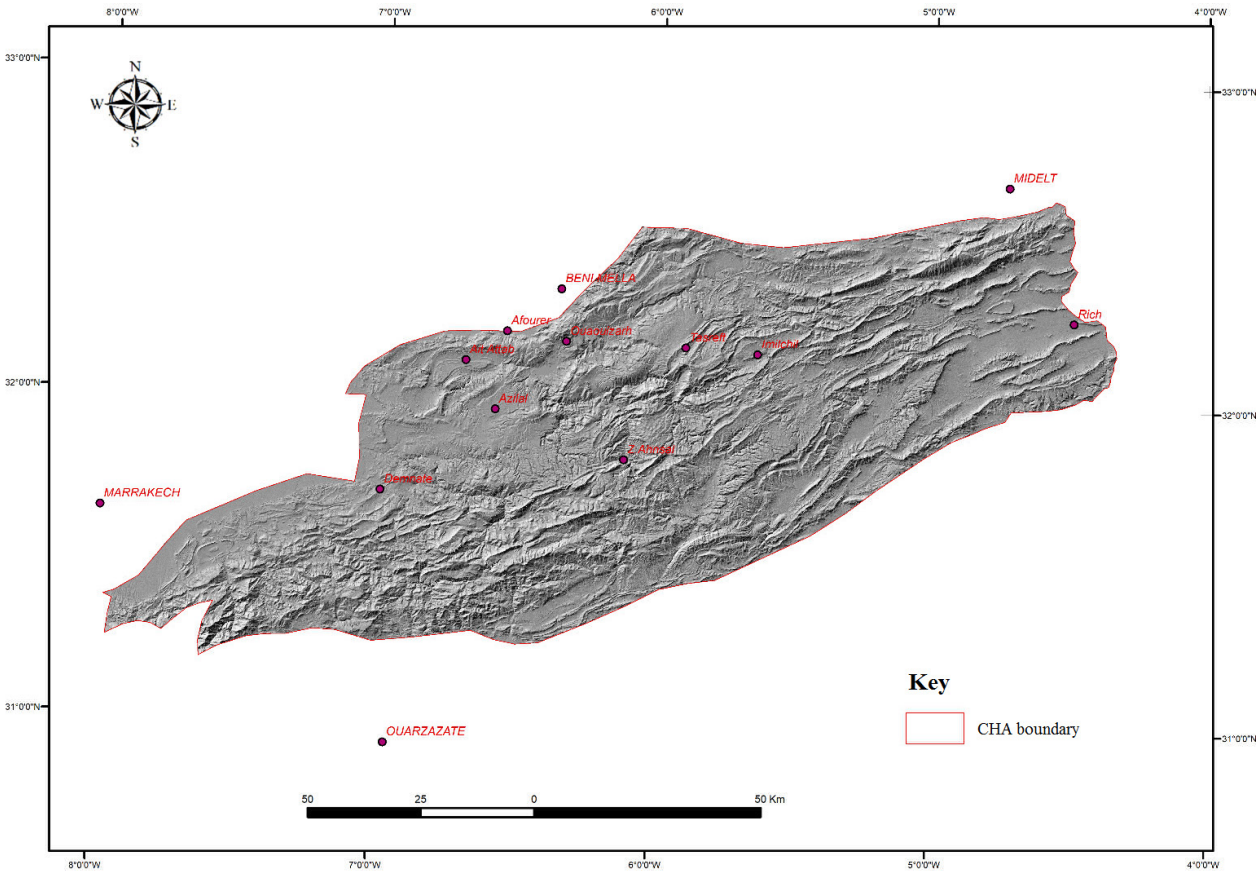

Figure 4.— Spacio-map of the Central High Atlas from Shaded Relief processing.

ter) data, It allows to generate images of the shaded relief (Figure 4) derived from the Digital Elevation Model (DEM) with a resolution of 30 meters with a directed illumination of the study area is carried out to better expose the shaded and unshaded areas (Adiri *et al.*, 2017) and the boundaries between the two areas can indicate the presence of lineaments (Li, 2010; Saadi *et al*., 2011).

The lineaments are detected in an automatic way using the PCI Geomatica Line algorithm that has been applied to the Landsat OLI filtered images and the shaded relief image. The obtained result is systematically completed by a visual inspection to map the lineaments not extracted by the automatic method, they were also checked before being retained to avoid confusing the elements that can be non-structural lineaments (road, railroad, wooded boundaries, cliffs).

Mapping the geometry of the lithological features

Lithological mapping is an important step in various mineral exploration studies as it forms the basis for the interpretation and validation of mining results. Lithological discrimination is done either in an automatic way using supervised machine learning algorithms such as SVM (Yu *et al.*, 2012; Othman & Gloaguen 2014 & 2017; Liu *et al.*, 2018) which is the most popular in lithological mapping using multispectral imagery or by traditional methods (Pournamdari *et al.*, 2014; Kumar *et al.*, 2015). In the case of our study, we chose to use satellite data to map lithological units in the Central High Atlas using the Principal Component Analysis method and the Optimal Index Factor method applied to multispectral data (Pournamdari *et al.*, 2014; Tabeliouna *et al.*, 2016; El Atillah *et al.*, 2018).

PCA is a method to improve the spectral signature of images, it is used to decrease the number of correlations between different bands and increase the differentiation between them. Principal component transformation generates new uncorrelated images, where the first component contains the maximum amount of information and the other components contain less and less information (Loughlin 1991; Bonn and Rochon, 1992; Jourda *et al.*, 2006). PCA has been applied to Landsat 8 OLI scenes to determine the best combination of bands for lithological mapping in the mitogenic zones of the Central High Atlas. This method has been used by several authors for lithology mapping (Crosta *et al*., 2003; Rowan and Mars, 2003; Ranjbar *et al*., 2004; Tangestani *et al*., 2008; Amer *et al*., 2010).

For the selection of the best band combinations for the discrimination of different lithological units, we also introduced the notion of Optimum Index Factor "OIF" defined by (Chavez *et al.*, 1982) as a statistical value applied to select the ideal combination of the three best bands of a satellite image, to create a composite that presents the most information with the least duplication (Qaid & Basavarajappa 2008; Berraki *et al.*, 2012; El Atillah *et al.*, 2018; El Atillah *et al.*, 2019). It is based on the calculations of correlation (Table 4) and variance-covariance (Table 5) matrices for simpler and more efficient interpretation and analysis of the combination whose highest OIF is

Table 4.— Correlation matrix of the seven principal components using the Landsat 8 OLI bands (2, 3, 4, 5, 6 and 7).

	Band1	Band2	Band3	Band4	Band5	Band6	Band7
Band1	1,0000						
Band2	0,97	1,0000					
Band3	0,98	0. 99	1,0000				
Band4	0,98	0. 98	0,97	1.000			
Band5	0,98	0. 98	0,99	9.97	1,0000		
Band6	0,87	0. 98	0,99	0.98	0,98	1,0000	
Band7	0.87	0.98	0.99	0.98	0,97	0,99	1,0000

Table 5.— Variance-covariance matrix of the seven principal components using the Landsat 8 OLI Bands (1, 2, 3, 4, 5, 6, and 7).

	Band 1	Band 2	Band 3	Band4	Band 5	Band6	Band7
Band 1		26367463,9	28351008,7	33433824,3	41747040,8	46847747,4	40792552
Band2		27357485,4	27552228,4	34423618,2	42569147,5	45678256,2	41587462,5
Band3		28351008,7	30663720,9	36385860,3	45133396,1	51062786,7	44515387,4
Band4		33433824,3	36385860,3	43736963,2	53702286,6	61475572	53681203,8
Band5		41747040,8	45133396,1	53702286,6	69399263,9	76904979,9	66083580,1
Band6		46847747,4	51062786,7	61475572	76904979,9	88944211,7	76906660,2
Band7		40792552	44515387,4	53681203,8	66083580,1	76906660,2	67267637,7

Table 6. Result of optimal index factor calculation (OIF).

Coloured compound	Red channel	Green channel	Blue channel	OIF
1	Band5	Band6	Band7	8830. 13
2	Band4	Band5	Band6	8292. 97
3	Band4	Band6	Band7	8164. 81
4	Band3	Band5	Band6	7938. 38
5	Band4	Band5	Band7	7895. 20

likely to provide the maximum lithological information (Table 6).

Mineralogical Mapping

The Central High Atlas contains some alterations linked to mineralization, the main ones being dolomitization associated with Zn-Pb-Fe and Ni-Cu mineralization, formed as a consequence of magnesian and ferriferous metasomatism affecting the host limestone of the mineralization (Mouguina, 2004). The clay complexes (smectite, corrensite, and chlorite) form as a result of the circulation of hydrothermal fluids that have already precipitated their metal stock (Zn, Pb, and Fe) and have become enriched in Si and Al (Inoue & Utada, 1991; Buatier *et al.*, 2002, 2004). The clay assemblages are marked by the occurrence of kaolinite whose content varies in parallel to that of the ore, which suggests that the emplacement of the kaolinite and the mineralization come from the common hydrothermal fluid (Mouguina & Daoudi, 2008). Calamine ores (Smithsonite, hemimorphite, hydrozincite, and cerussite) of supergene origin associated with iron oxides and hydroxides (goethite, limonite, and hematite) are formed by direct replacement of mineralized bodies (sphalerite and galena) or by filling cavities along fractures associated with compression of the atlas (Chaulet *et al.*, 2014) Carbonates and hydrocarbons (copper, malachite, azurite) are secondary minerals formed as a result of the supergene alteration of red Cu and Fe deposits and are associated with other secondary minerals such as iron oxides and hydroxides (hematite, goethite, limonite) (Ibouh *et al.*, 2011).

The calculation of alteration mineral occurrences in the Central High Atlas is a process that can be

Table 7.— Some examples of alteration mineral ratios and index under Landsat OLI 8, Sentinel 2 and Aster images (Kalinowski and Oliver, 2004; Van der Werff & van der Meer 2016).

Minerals	Landsat OLI	Sentinel 2	Aster
Clay minerals	6/7	11/12	4/(5,6,7)
Ferrous minerals	5/3+1/2	7/5+3/4	12/8+3/4
Iron oxide	4/3	4/3	2/1
Ferrous silicates	5/3+1/2	7/5+3/4	12/8+3/4
Alteration	5/7+4/2+5/4	11/12	4/5

Table 8.— Some examples of weathering mineral ratios under Aster images (Gozzard, 2006).

Minerals	Ratios
Alunite, Kaolinite, Pyrophyllite	(4+6)/5
Carbonate, Chlorite, Epidote	(7+9)/8
Dolomite	(6+8)/7
Kaolinite	7/5
MgOH, Carbonate	(6+9)/8
Muscovite	7/6
Phengite	5/6
Quartz abundance	13/10
Sericite, Muscovite, Illite, Smectite	(5+7)/6
Vegetation	(3–2)/(3+2)

completed in the study and research phase for mineral explorations. Some types of alteration can be better distinguished by remote sensing than in the field, as most minerals have absorption characteristics at wavelengths outside the spectrum visible to the human eye. For this reason, we have opted to calculate band ratios (Kalinowski and Oliver, 2004; Gozzard, 2006; Van der Meer *et al.*, 2014) on Aster, Landsat OLI, and Sentinel 2 bands (Tables 7 and 8), which is a very useful technique to detect areas with spectral anomalies of minerals or mineral groups associated with the presence of hydrothermal or supergene alteration in the study area (Van der Werff & Van der Meer, 2016; El Atillah *et al.,* 2018; Adiri *et al.*, 2020).

Results and Discussion

The interpretation of the results of the directional filter processing (3x3 matrix) applied on the near-infrared band of the Landsat 8 OLI image (Figure 11), corresponding to our study area, shows two different direction families N130-N140 and E-W (Figures 5 & 6) with a major direction N70-N90 (Figure 7), while the application of the directional filters (7x7 matrix) reveals the main family of N-S direction (Figure 8). On the other hand, the interpretation of the lineaments extracted by the shaded relief method indicates a single lineament family with an N45 to N70 direction (Figure 9). The comparison of the lineaments extracted from the Landsat images and the shaded relief with those extracted from the geological map of the study area showed a certain resemblance. Indeed, the majority of the faults and seams validated by remote sensing maintain a general direction from N45 to N70 and the second direction of NNE-SSW and These directions are the same as those extracted from the geological map of the study area (Figure 12).

The combination of the four lineament maps, derived from the three previously mentioned methods, was done in a GIS environment to remove duplicate lineaments which will provide a global map of the CHA lineaments (Figure 9) with a lineament direction that is predominantly NE-SW and E-W with a predominance of NNE-SWSW and ENE-WSW.

Density of lineaments

In lineament studies, density is a widely used parameter (Lachaine, 1999; Corgne *et al.*, 2010;

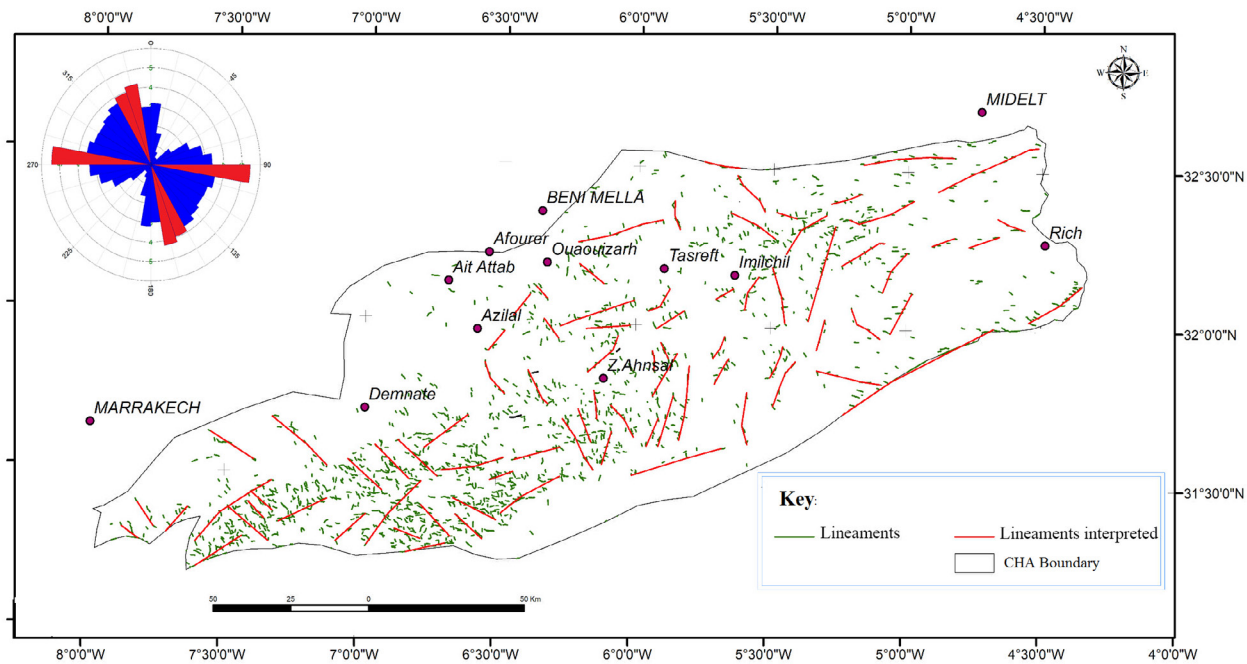

Figure 5.— Lineament map from the 3x3 directional filter (NW-SE) and its directional rose.

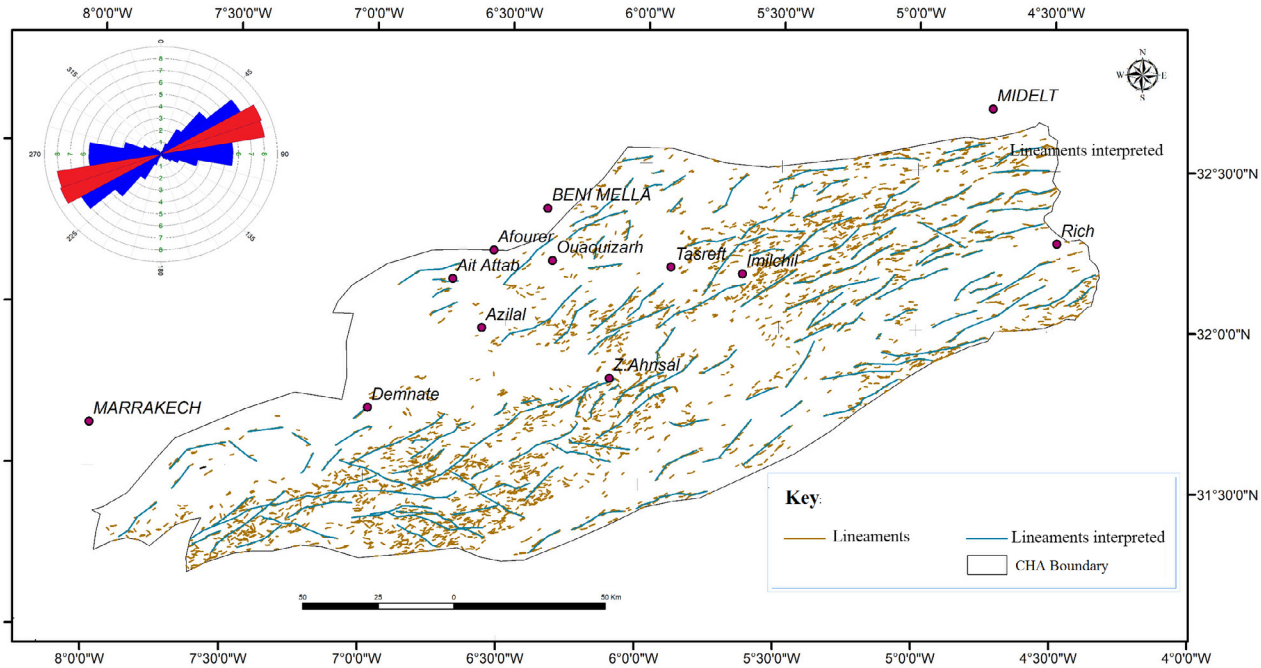

Figure 6.— Lineament map from the 3x3 directional filter (90 E) and its directional rose.

Hashim *et al.*, 2013). It gives information concerning the concentration of lineaments per unit area (Lachaine, 1999). In the present work, the fracture density map indicates three intense zones (Figure 13); The highest concentrations of lineaments are found south of Demnat, corresponding to about half a dozen N70-trending faults (Le Marrec & Jenny, 1980; Jenny & Jossen, 1982) that are marked in the High Atlas basement south of Demnate. On the other hand, in the Imlchil region (eastern part), there is a lower concentration of lineaments that coincide with magmatic rifts.

The comparison of the directions of these lineaments to previous work shows a good correlation. The structures of the Central High Atlas generally follow two main directions; one is E-W to ENE-WSW and the other NNE-SSW. The main reverse fault anticlines mark the E-W / ENE-WSE direction and these same directions delineate the High Atlas trough as a whole and are recognizable throughout the Maghreb (Bentahr *et al.*, 2020; El Moujahid *et al.*, 2016). They thus characterize the structures, related to the evolution of the southwestern termination of the Tethys. The other direction, NNE-SSW, is emphasized by faults that limit the eruptive rock

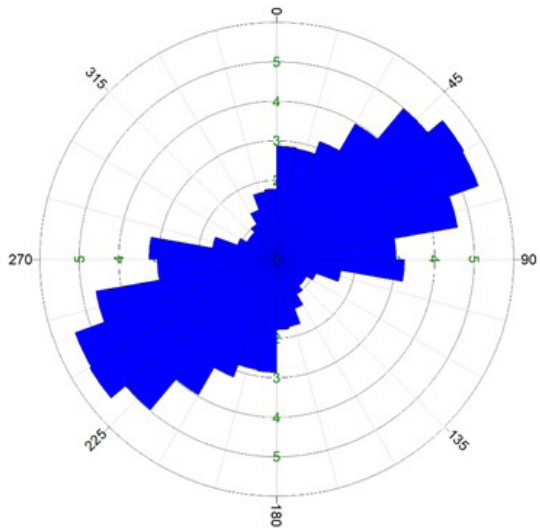

Figure 7.— Global Directional Rose of 3x3 lineaments.

complexes and by secondary anticlines that connect the main chains (Nouayti *et al.*, 2017). In addition, the edges of some basins filled with the Jurassic Red series follow the same direction. This direction is strongly related to the development of the Atlantic (Hinz *et al.*, 1982), these same directions are exactly the main threads of the deformations attributed to the Hercynian orogeny (Proust & Tapponnier, 1973;

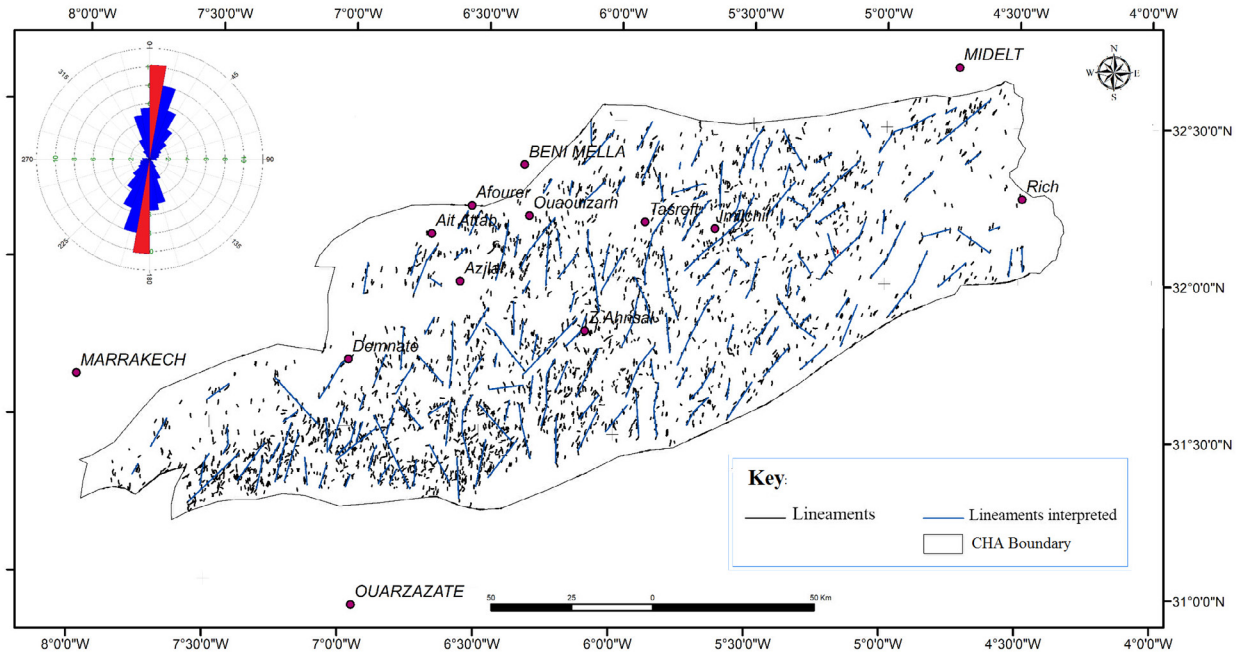

Figure 8.— Lineament map from the directional filter 7x7 (N-S) and its directional rose.

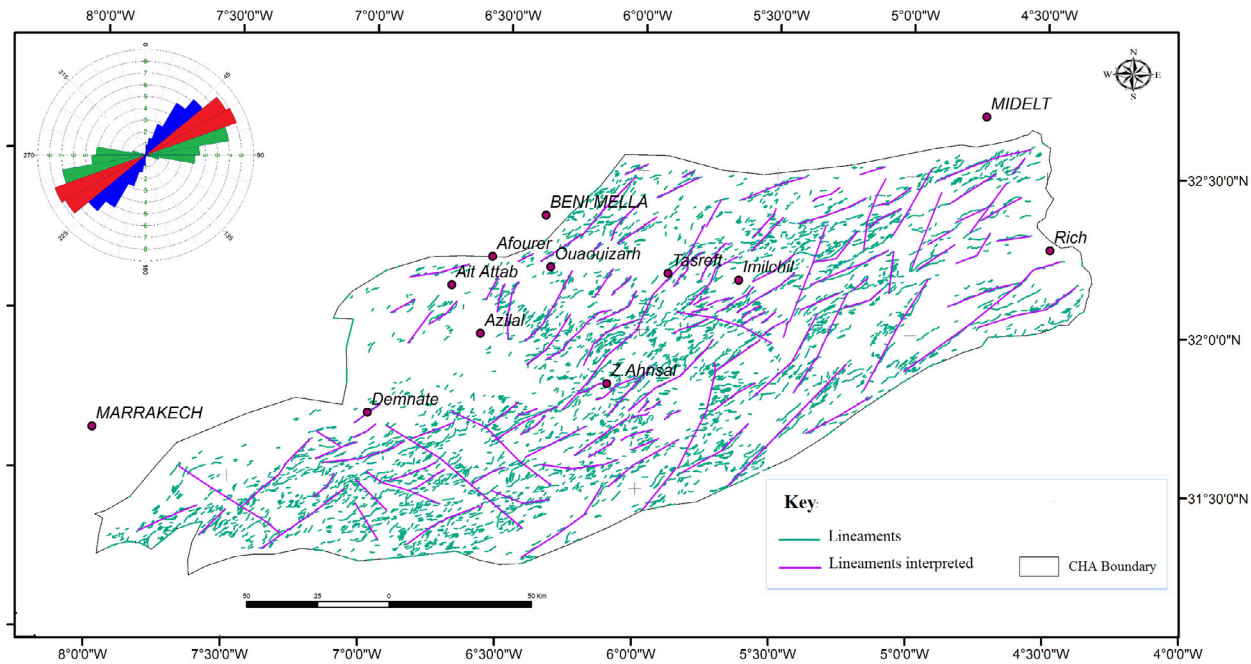

Figure 9.— Lineament map from the Shaded Relief treatment and its directional rose.

Michard, 1976, Benammi *et al.*, 2001), but they are already identified in an older structuring phase, which belongs to the Pan-African orogeny and influences the development of the North-Western African margin during the Paleozoic (Piqué, 1979). The results of this work indicate that the use of various satellite data by applying the automatic extraction of lineaments allows the detection of different families

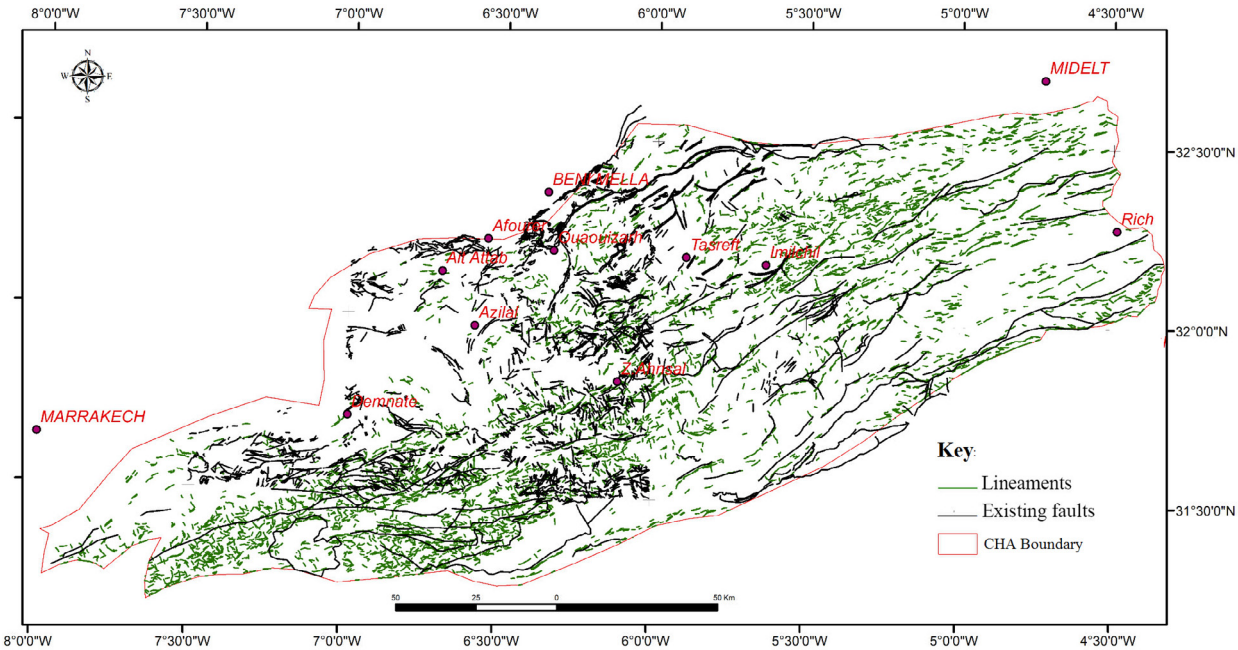

Figure 10.— Map of all interpreted lineaments in the Central High Atlas study area.

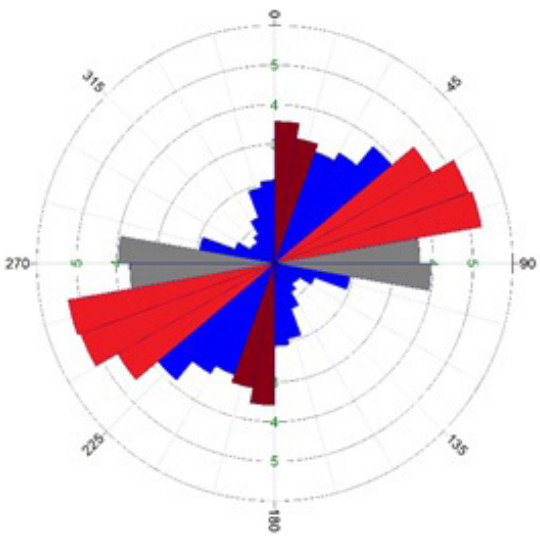

Figure 11.— The fault direction rose from the Landsat 8 OLI image.

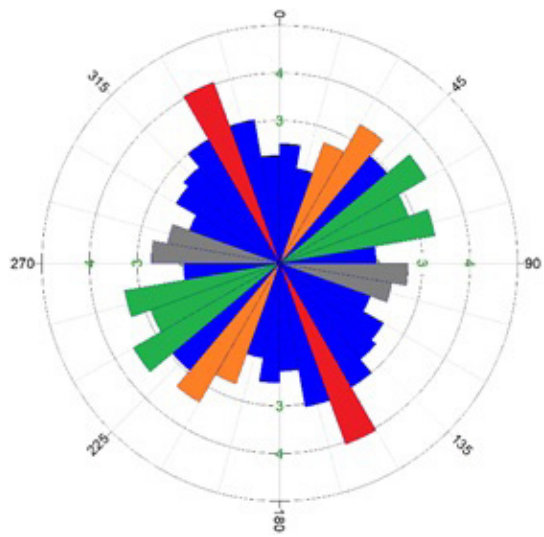

Figure 12.— Rose of the fault directions from the geological map.

of fractures to understand the influence of the Alpine orogeny in the Central High Atlas.

Mapping the geometry of the lithological features

The realization of the lithological map is a fundamental step in the lithostructural and mining studies, it constitutes the basis for the interpretation and validation of the obtained results. In this work, the mapping of lithological classes was carried out using PCA and OIF because of their effectiveness in the lithological mapping of AMP (Figures 14 & 15). Therefore, the statistical calculation of the PCA shows that the RGB composite colors of the Landsat OLI data (PC1, PC2, PC3) contain more than 98% of the information with a clear visualization of the

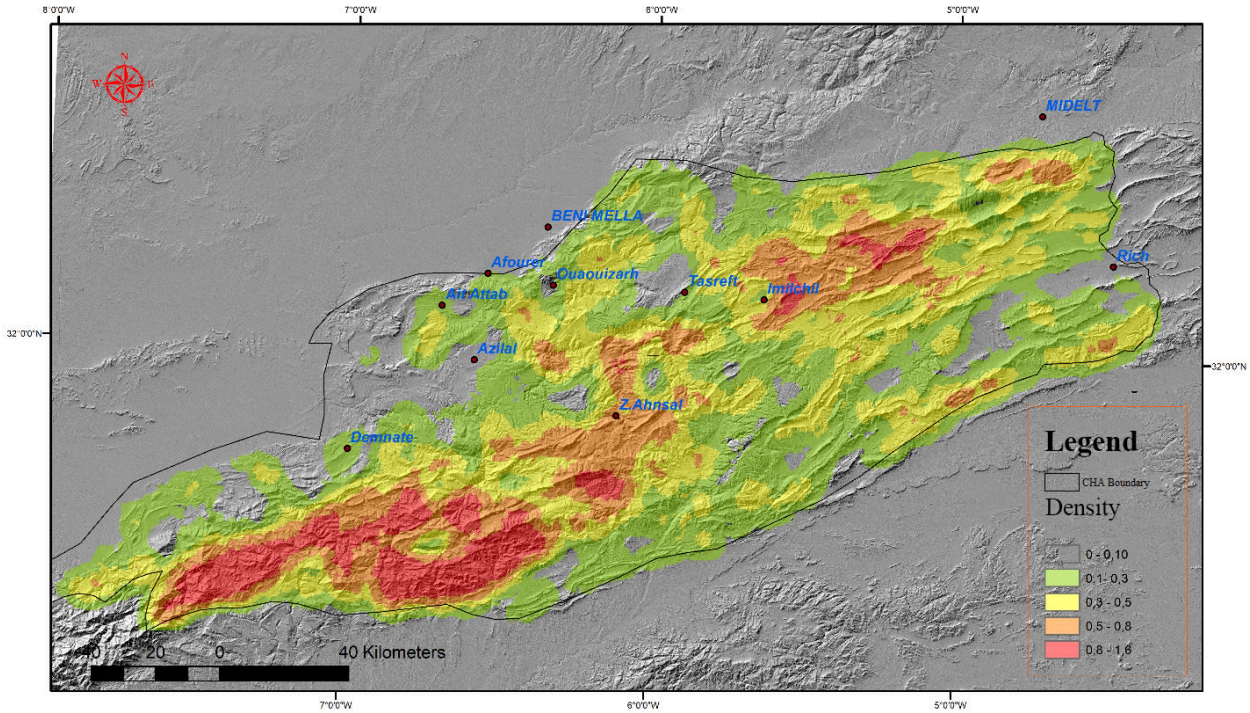

Figure 13.— Lineament density map of the Central High Atlas study area.

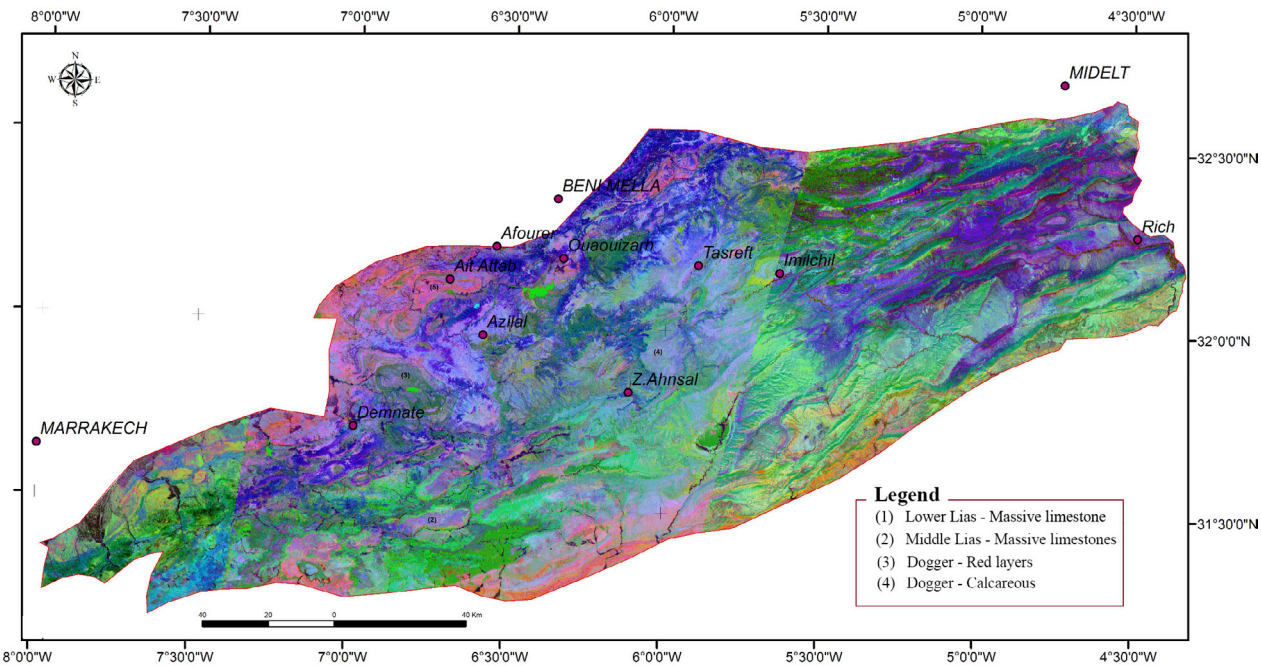

Figure 14.— Spacio-map of the processing Principal Component Analysis (PCA).

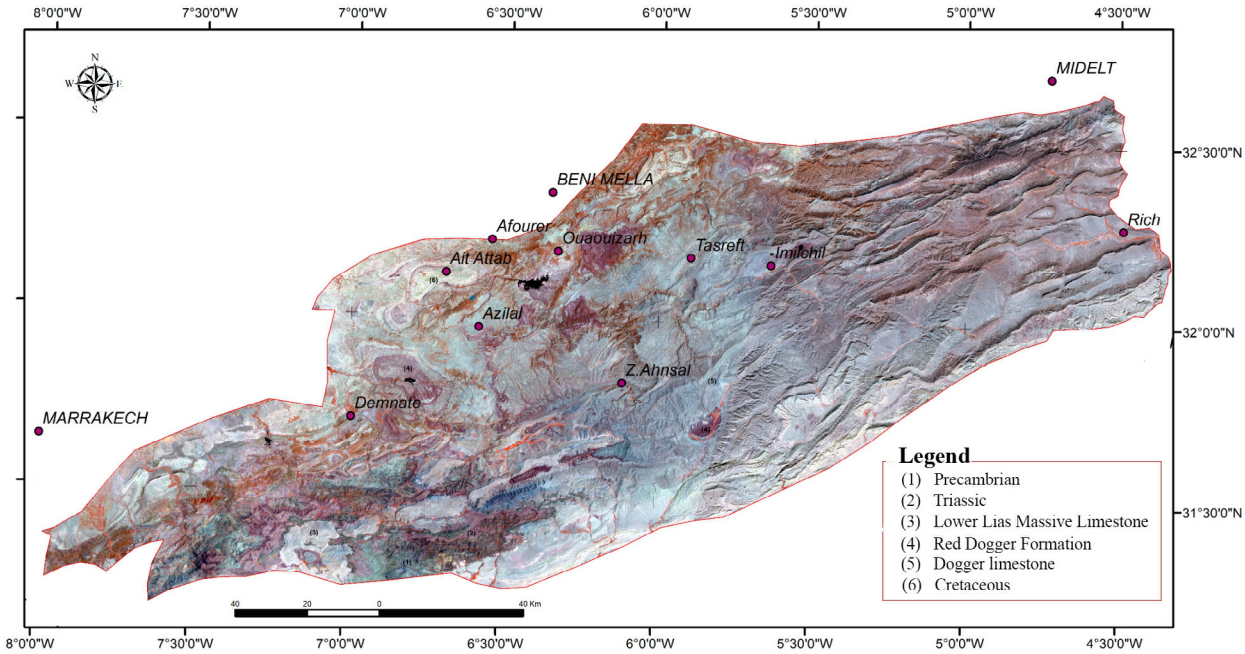

Figure 15.— Spacio-map of the colored compound of uncorrelated bands 5, 6, and 7 of the OIF.

relief boundaries, which allowed us to discriminate the different units of massive limestone, Lawer and Middle Lias, Dogger and limestone.

The different analyses of all the OIF values indicate that the optimal combination of bands 5, 6, and 7 among all the possible combinations, corresponding to the highest OIF value (8830, 13) Table 6, is the most suitable for geological mapping. It is likely to provide more lithologic information, differentiate the spectral signatures of lithologic units, and highlight the boundaries of Precambrian, Triassic, Lower Liassic Massive Limestone, Red Dogger Formation, Dogger Limestone, and Cretaceous rock units.

These results show that the lithologic mapping obtained by both techniques correlates well with the geologic map (Figure1) and the work done in the study area (Teixell *et al*., 2017). This shows that the proposed methodology demonstrates a high potential of Landsat 8 OLI data in the discrimination of lithological units (Rowan & Mars 2003; Adiri *et al.*, 2016; Boettinger *et al.*, 2018; Ourhzif *et al.*, 2019).

Mineralogical mapping of the Central High Atlas

The analysis of the results of the processing of indices under Landsat OLI image of the Central High Atlas massif allows us to identify the distribution of minerals in three zones (Figure 16); the most important one is located east of Imilchil, the second one is situated south of Demnate and the third zone is focused north of Zaouiat Ahnsal. Generally speaking, the central part of the Central High Atlas (Imilchil, Talmeste, and Tansref) is the one that presents a richness in ferrous clay minerals and iron oxides and is also characterized by an apparent hydrothermal alteration. Clay minerals are most often located in the Oueds, which is probably due to drainage by the waters at the time of the floods, and stabilize in the topographically low areas, meaning that the clay minerals located at the level of the Oueds are not necessarily alterations, whereas at the level of the magmatic ripples the clay alteration is remarkable. The iron oxides are organized along oxidation corridors oriented in the direction of the large N70 structures of the Central High Atlas. For the ferrous minerals, their analysis shows three important zones; the first is located in the northern part at the level of the red formations of the Jurassic-Cretaceous age (sandstones and red pelites), the second is to the south of Demnate, on the altered basaltic formations of the Triassic and the last one is situated in the central and eastern part at the level

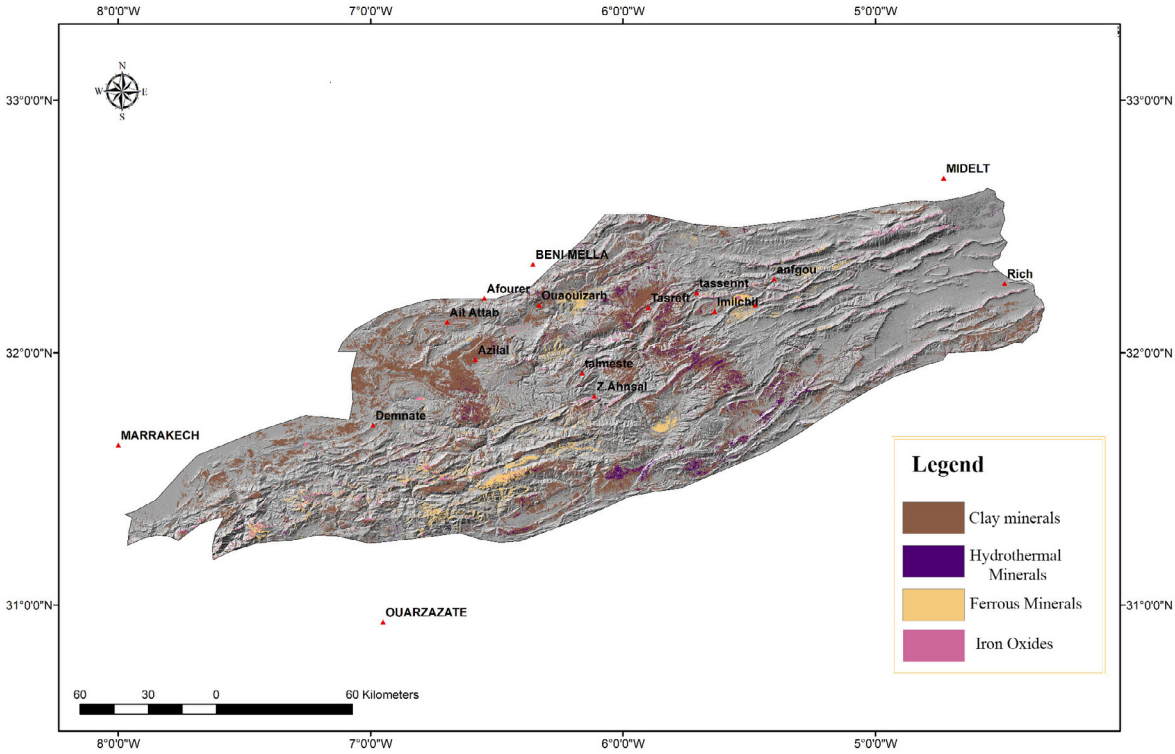

Figure 16.— Map of indices made on the Landsat OLI 8 image of the Central High Atlas.

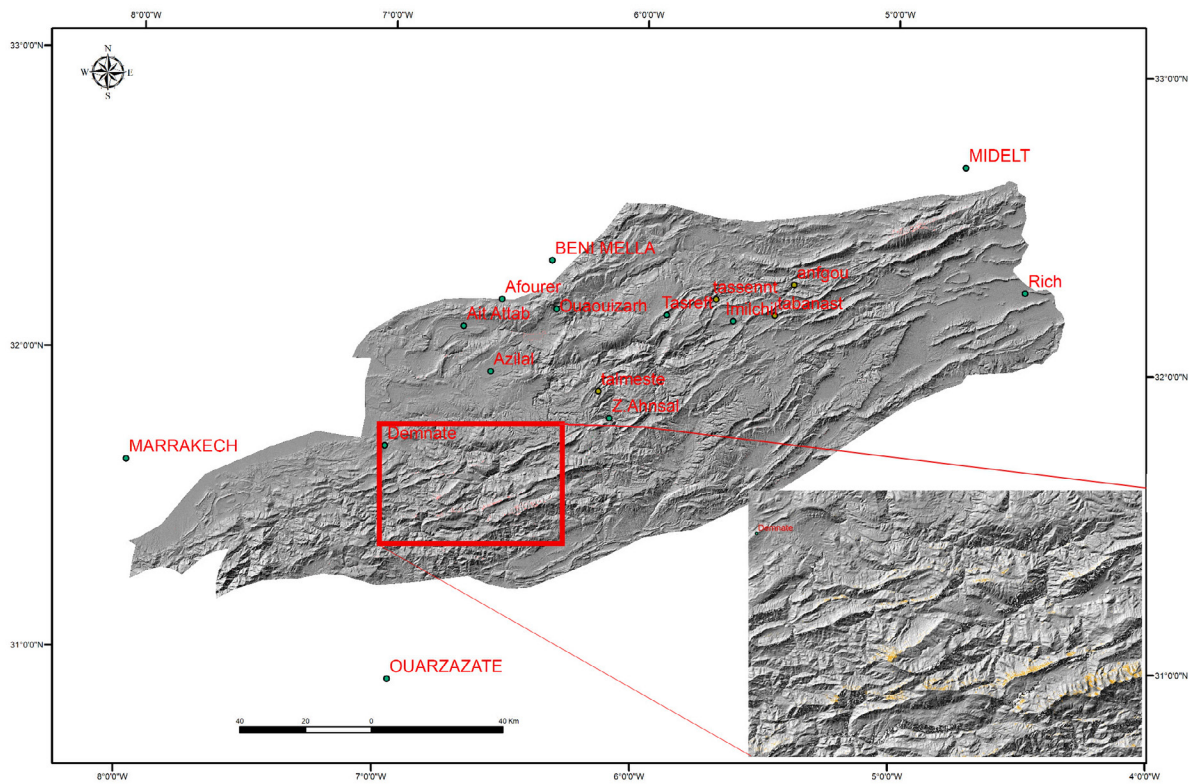

Figure 17.— Spatial index map of the Ferrous Minerals of the Central High Atlas.

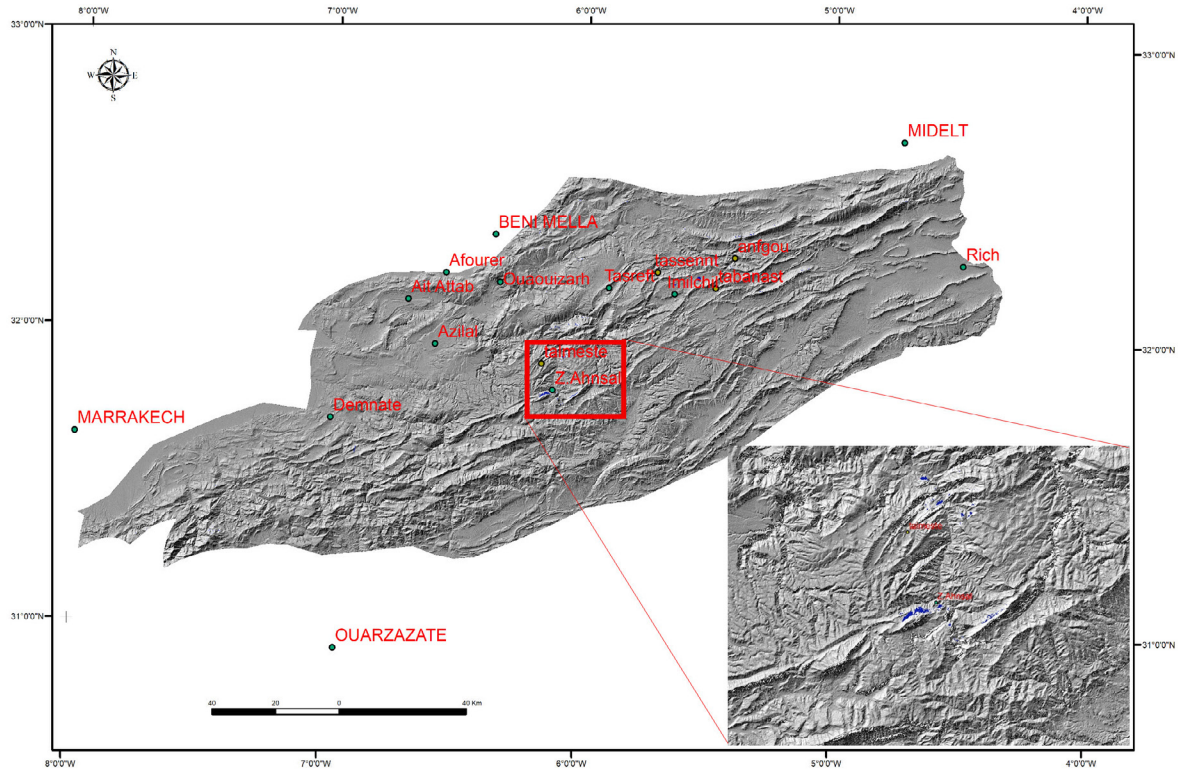

Figure 18.— Spatio-map of the Cay Minerals of the Central High Atlas.

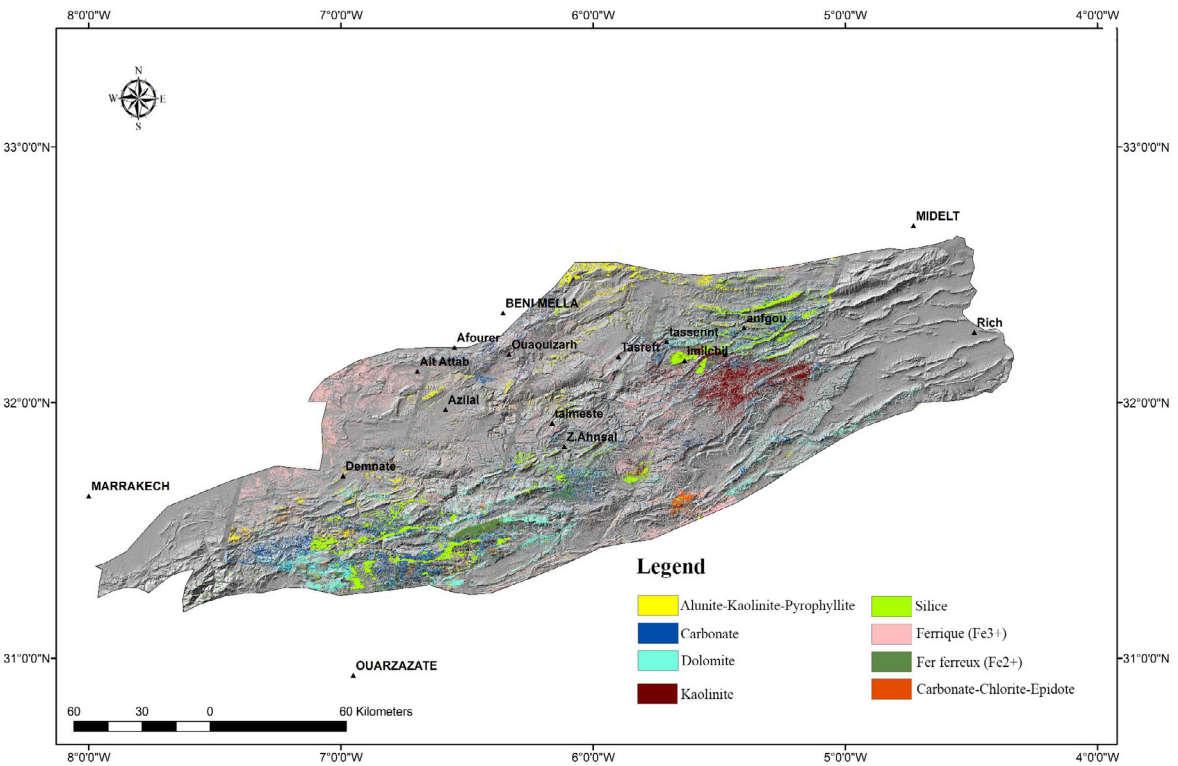

Figure 19.— Map of the indices carried out on the Aster image of the Central High Atlas.

of the magmatic wrinkles. The hydrothermal alteration minerals are located in the central part at the level of the magmatic ripples.

The calculation of the ratios between the bands under the Sentinel 2 image, allowed us to highlight two types of alteration mineral indices (Figures 17 & 18); the clay minerals which are localized in the west of Zaouiat Ahnsal and in the north of Anfgou which present elongated forms oriented NE-SW and the iron minerals in the south of Demnat, they show a NE-SW orientation.

The spatial maps of the indices under the Aster image (Silica, Dolomite, Carbonate, Carbonate-chlorite-epidote, Alunite-kaolinite-pyrophyllite, Kaolinite, Ferrous minerals, and Iron oxide) quoted below, obtained by processing Aster images were superimposed to see the spatial relationship between the different anomalies detected. The results obtained in (Figure 19) show a certain similarity with the map of indices extracted from Landsat OLI images (Figure 16). The most important areas are located in the southern part of Demnate and the others in the central part (Imlchil).

The arrangement of the different indices such as Silica, Dolomite, Carbonate, Alunite-kaolinite-pyrophyllite, Carbonate-chlorite-epidote, Kaolinite, and Iron minerals generally shows a tendency to appear in groups, while iron oxides appear in both areas and also at the level of the syncline of Ait Aattab. By way of explanation, we can suppose the existence of a hydrothermal system that controls the alterations, especially those that are elongated. According to the studies that have been done in the region (Chèvremont, 1975; Mouguina, 2004; Ibouh *et al.*, 2011), these alterations are linked to the setting of Jurassic magmatic intrusions.

Conclusions

This study presents the integration of multispectral and hyperspectral data from Aster, Landsat 8OLI, and Sentinel 2 sensors, for the mapping of hydro-thermal alteration minerals associated with a mapping of the fraction of the Central High Atlas. The realization of the map of the fractures of the Central High Atlas was made possible by the use of techniques of analysis of satellite images Landsat 8 OLI and Aster GDEM, to identify the networks of lineaments affecting the area and which are divided into three major families of direction; NE-SW to E-W with a predominance of NNE-SWSW and ENE-WSW. This distribution of structural lineaments is relative to the alpine orogeny dynamics and the rate of deformation of the alpine orogeny in the study area.

The Landsat 8 OLI, Sentinel 2, and Aster satellite images are also used to establish mineralization maps of the Central High Atlas as an essential remote sensing tool in the field of mineral prospecting. The analysis of these maps shows two potential areas to be targeted in the field for further study; the first area is located south of Demnate, at the southwestern end of the Central High Atlas, which reveals silica, dolomite, carbonate, carbonate-chlorite-epidote, iron minerals, clay minerals, iron oxide, and alunite-kaolinite-pyrophyllite alterations and occupies a significant area on the Stepha-no-Triassic formations. The second area is located in the central part of the Central High Atlas where the most abundant alterations are carbonation and dolomitization, which cover vast areas; their comparison with the geological map shows diffusion of these two phenomena on the carbonate formations of the dogger.

The integration of the metalliferous indices and fault extracted from the geological maps with the resulting alteration and lineament maps shows a better correlation which confirms the effectiveness of GIS and remote sensing techniques in structural and mineralogical geology studies. The superposition of the alteration maps with the lineament map results in a concluding map that shows that the potential alteration zones are affected by NE-SW oriented faults. This final alteration and fracture map are considered a basic starting point for mineral exploration in the Central High Atlas.

References

Adiri, Z.; El Harti, A.; Jellouli, A.; Lhissou, R.; Maacha, L.; Azmi, M.; Zouhair, M. & Bachaoui, E.M. (2017). Comparison of Landsat-8, ASTER and Sentinel 1 satellite remote sens-ing data in automatic lineaments extraction: A case study of Sidi Flah-Bouskour in-lier, Moroccan Anti Atlas. Advances in Space Research, 60(11): 2355-2367. https://doi.org/10.1016/j.asr.2017.09.006

Adiri, Z.; El Harti, A.; Jellouli, A.; Maacha, L. & Bachaoui, E.M. (2016). Lithological mapping using

Landsat 8 OLI and Terra ASTER multispectral data in the Bas Drâa inlier, Moroccan Anti Atlas. Journal of Applied Remote Sensing, 10(1): 016005. https://doi.org/10.1117/1.JRS.10.016005

Adiri, Z.; El Harti, A.; Jellouli, A.; Maacha, L.; Azmi, M.; Zouhair, M. & Bachaoui, E.M. (2020). Mineralogical mapping using Landsat-8 OLI, Terra ASTER and Sentinel -2A multispectral data in Sidi Flah-Bouskour inlier, Moroccan Anti-Atlas. Journal of Spatial Science, 65(1): 147-171. https://doi.org/10.1080/14498596.2018.1490213

Ait Addi A. & Chafiki D. (2013). Sedimentary evolution and palaeogeography of mid-Jurassic deposits of the Central High Atlas, Morocco. Journal of African Earth Sciences, 84: 54-69. https://doi.org/10.1016/j.jafrearsci.2013.04.002

Ait Inoh, H.; Tayebi, M. & Rajji, A. (2022). Contribution of Remote Sensing and GIS to Identify the Potential Area for Artificial Recharge in Fractured Area in the Talmakent Region, Western High Atlas, Morocco. Journal of Environmental and Agricultural Studies, 3(1): 24-36. https://doi.org/10.32996/jeas.2022.3.1.3

Alhirmizy, S. (2015). Automatic mapping of lineaments using shaded relief images de-rived from Digital Elevation Model (DEM) in Kirkuk Northeast Iraq. International Journal of Science and Research, 4(5): 2228-2233.

Alshayef, M.S. & Javed, A. (2018). Geomatica-Based Approach for Automatic Extraction of Lineaments from ASTER-GDEM Data, in Part of Al-Rawdah, Shabwah, South-east Yemen. In Hydrologic Modeling (Vijay P Singh, Shalini Yadav & Ram Narayan Yadava, Eds.), 81: 423-434. https://doi.org/10.1007/978-981-10-5801-1_29.

Amer, R.; Kusky, T. & El Mezayen, A. (2012). Remote sensing detection of gold related alteration zones in um rus area, central eastern desert of Egypt. Advances in Space Research, 49: 121-134. https://doi.org/10.1016/j.asr.2011.09.024

Azizi, H.; Tarverdi, M.A. & Akbarpour, A. (2010). Extraction of hydrothermal alterations from ASTER SWIR data from east Zanjan, northern Iran. Advances in Space Research, 46: 99-109. https://doi.org/10.1016/j.asr.2010.03.014

Bentahar, I.; Raji, M. & Si Mhamdi, H. (2020). Fracture network mapping using Landsat-8 OLI, Sentinel-2A, ASTER, and ASTER-GDEM data, in the Rich area (Central High Atlas, Morocco). Arabian Journal of Geosciences, 13(16): 1-19. https://doi.org/10.1007/s12517-020-05736-6

Berraki, F.; Bendaoud, A.; Brahmi, B.; Djemai, S.; Kienast, J.; Deroin, J. & Ouzegane, K. (2012). Cartographie et étude pétrographique et minéralogique des dykes de dolérites de l'In Ouzzal (Hoggar occidental, Algérie). Photo-Interpretation. European Journal of Applied Remote Sensing, 2012/1: 2.

Boettinger, J.L.; Ramsey, R.D.; Bodily, J.M.; Cole, N.J.; Kienast-Brown, S.; Nield, S.J. & Stum, A.K. (2008). Landsat spectral data for digital soil mapping. In: Digital soil mapping with limited data (Hartemink, A.E.; McBratney, A. & Mendonça-Santos, M.D. Eds.) (pp. 193-202). Springer, Dordrecht. https://doi.org/10.1007/978-1-4020-8592-5_16

Bolouki, S.M.; Ramazi, H.R.; Maghsoudi, A.; Beiranvand Pour, A. & Sohrabi, G. (2019). A remote sensing-based application of Bayesian networks for epithermal gold potential mapping in Ahar-Arasbaran Area, NW Iran. Remote Sensing, 12(1): 105. https://doi.org/10.3390/rs12010105

Bonn, F. & Rochon, G. (1992). Précis de télédétection. Volume 1: principes et méthodes. Presses de L'Université du Québec, Québec, 485 pp.

Brede, R.; Hauptmann, M. & Herbig, H.G. (1992). Plate tectonics and intracratonic moun-tain ranges in Morocco-The Mesozoic-Cenozoic development of the Central High Atlas and the Middle Atlas. Geologische Rundschau, 81(1): 127-141. https://doi.org/10.1007/BF01764544

Brunet, M.F. & Cloetingh, S. (2003). Integrated peri-Tethyan basins studies (peri-Tethys programme). Sedimentary Geology, 156(1-4): 1-10. https://doi.org/10.1016/S0037-0738(02)00279-8

Buatier, M.D.; Guillaume, D.; Wheat, C.G.; Hervé, L. & Adatte, T. (2004). Mineralogical characterization and genesis of hydrothermal Mn oxides from the flank of the Juan the Fuca Ridge. American Mineralogist, 89(11-12): 1807-1815. https://doi.org/10.2138/am-2004-11-1227

Buatier, M.D.; Karpoff, A.M. & Charpentier, D. (2002). Clays and zeolite authigenesis in sediments from the flank of the Juan de Fuca Ridge. Clay Minerals, 37(1): 143-155. https://doi.org/10.1180/0009855023710024

Chabane, S.; Amri, K. & Hamdidouche, R. (2019). Deformation Pattern in the El Ahmar Area (Bechar Basin, Southwestern Algeria): Contribution of Lansat 8 OLI and Field Measurement. Arabian Journal of Geosciences, 12 (5): 158. https://doi.org/10.1007/s12517-019-4311-6

Chacrone, C. & Hamoumi, N. (2005). L'Arenig-Llanvirn du Haut Atlas occidental et cen-tral (Maroc). Environnements sédimentaires, paléogéographie et contrôle de la sédimentation. Comptes Rendus Geoscience, 337(12): 1026-1034. https://doi.org/10.1016/j.crte.2005.05.015

Chavez Jr, P.S. (1982). US Geological Survey mini image processing system (MIPS) (No. 84-880). US Geological Survey.

Chevremont, P. (1975). Les roches eruptives basiques des boutonnieres de Tassent et Tasraft et leurs indices metalliferes dans leur cadre geologique, Haut-Atlas Central, Maroc. PhD Thesis, Université Claude Bernard Lyon I, 148 pp.

Corgne, S.; Magagi, T.; Yergeau, M. & Daouda, S. (2010). An Integrated Approach to Hy-dro-Geological Lineament Mapping of a Semi-Arid Region. Remote Sensing of Environment, 114(9): 1863-1875. https://doi.org/10.1016/j.rse.2010.03.004

Crosta, A.P.; De Souza Filho, C.R.; Azevedo, F. & Brodie, C. (2003). Targeting key al-teration minerals in epithermal deposits in Patagonia, Argentina, using ASTER imagery and principal component analysis. International Journal of Remote sensing, 24(21): 4233-4240. https://doi.org/10.1080/0143116031000152291

Drusch, M.; Del Bello, U.; Carlier, S.; Colin, O.; Fernandez, V.; Gascon, F.; & Bargellini, P. (2012). Sentinel 2: ESA's optical high-resolution mission for GMES operational services. Remote Sensing of Environment, 120: 25-36. https://doi.org/10.1016/j.rse.2011.11.026

El Atillah, A.; Zine El Abidine, E.L. & Souhassou, M. (2019). Utilisation de l'image mul-tispectrale Landsat 7 et 8 pour l'exploration minière: Cas de la boutonnière de Bou-Azzer-El Graara, Maroc. International Journal of Innovation and Applied Studies, 28(1): 299-315.

El Atillah, A.; El Morjani, Z.E.A. & Souhassou, M. (2018). Utilisation De L'image Multi-spectrale Pour L'exploration Et La Recherche Des Ressources Minérales: État Des Connaissances Et Proposition D'un Modèle De Traitement. European Scientific Journal, ESJ, 14(24), 350. https://doi.org/10.19044/esj.2018.v14n24p350

Fadile, A. (1987). Structure et évolution alpine du Haut Atlas central sur la transversale Agh-bala-Imilchil (Maroc). PhD Thesis, Université de Toulouse.

El Moujahid, H.E.A.; Ibouh, H.,; Bachnou, A.; Babram, M.A. & El Harti, A. (2016). Mapping and analysis of geological fractures extracted by remote sensing on Landsat TM images, example of the Imilchil-Tounfite area (Central High Atlas, Morocco). Estudios Geológicos, 72(2): e051. https://doi.org/10.3989/egeol.42328.394

Essaifi, A. & Zayane, R. (2018). Petrogenesis and origin of the Upper Jurassic-Lower Cre-taceous magmatism in Central High Atlas (Morocco): major, trace element and iso-topic (Sr-Nd) constraints. Journal of African Earth Sciences, 137: 229-245. https://doi.org/10.1016/j.jafrearsci.2017.10.002

Ettaki M, Chellaï EH, Milhi A, Sadki D, Boudchiche L (2000) Le passage Lias moyen-Lias supérieur dans la région de Todrha-Dadès: événements bio-sédimentaires et géodynamiques (Haut Atlas central, Maroc). Comptes Rendus de l'Académie Des Sciences - Series IIA - Earth and Planetary Science, 331(10): 667-674. https://doi.org/10.1016/S1251-8050(00)01458-0

Fossati, M.; Zerilli, A.; Ronchini, G. & Apolloni, B. (1992). Lineaments analysis for po-tential-fields data using neural networks. SEG Technical Program Expanded Abstracts, 6-9. https://doi.org/10.1190/1.1822192

Gabr, S.; Ghulam, A. & Kusky, T. (2010). Detecting areas of high-potential gold mineral-ization using ASTER data. Ore Geology Reviews, 38: 59-69. https://doi.org/10.1016/j.oregeorev.2010.05.007

Giese, P. & Jacobshagen, V. (1992). Inversion tectonics of intracontinental ranges: High and Middle Atlas, Morocco. Geologische Rundschau, 81(1): 249-259. https://doi.org/10.1007/BF01764553

Gozzard, J.R. (2006). Image processing of ASTER multispectral data. Geological Survey of WA, 51 pp.

Haddoumi, H.; Charrière, A. & Mojon, P.O. (2010). Stratigraphie et sédimentologie des «Couches rouges» continentales du Jurassique-Crétacé du Haut Atlas central (Maroc): implications paléogéographiques et géodynamiques. Geobios, 43(4): 433-451. https://doi.org/10.1016/j.geobios.2010.01.001

Haddoumi, H.; Charrière, A.; Feist, M.; Andreu B (2002). Nouvelles datations (Hauterivien supérieur-Barrémien inférieur) dans les «Couches rouges» continentales du Haut Atlas central marocain; conséquences sur l'âge du magmatisme et des structurations mésozoïques de la chaîne Atlasique. Comptes Rendus Palevol 1(5): 259-266. https://doi.org/10.1016/S1631-0683(02)00039-8

Hailwood, E.A. & Mitchell, J.G. (1971). Palaeomagnetic and radiometric dating results from Jurassic intrusions in South Morocco. Geophysical Journal International, 24(4): 351-364. https://doi.org/10.1111/j.1365-246X.1971.tb02183.x

Hashim, M.; Ahmad, S.; Johari, M.A. & Pour, A.B. (2013). Automatic lineament extraction in a heavily vegetated region using Landsat Enhanced Thematic Mapper (ETM+) imagery. Advances in Space Research, 51: 874-890. https://doi.org/10.1016/j.asr.2012.10.004

Hinz, K.; Dostmann, H. & Fritsch, J. (1982). The continental margin of Morocco: seismic sequences, structural elements and geological development. In: Geology of the Northwest African continental margin (Rad, U.; Hinz, K.; Sarnthein, M. & Seibold, E., Eds.). Springer, Berlin. 34-60. https://doi.org/10.1007/978-3-642-68409-8_3

Ibouh, H. & Mouguina. E.M. (2011). Aguerd n'Tazoult, une mine Zn-Pb du Haut Atlas Central. Notes et Memoires du Service Geologique, 564: 293-296.

Ibouh, H. (1995). Tectonique en décrochement et intrusions magmatiques au jurassique: tectogenèse polyphasée des rides jurassiques d'Imilchil (Haut Atlas central, Maroc). PhD thesis, Université Cadi Ayyad, Marrakech, Morocco, 225 pp.

Ibouh, H.; El Bchari, F.; Bouabdelli, M.; Souhel, A. & Youbi, N. (2001). L'accident tizal-azourki haut atlas central du maroc: déformations synsedimentaires liasiques en extension et conséquences du serrage atlasique. Estudios Geologicos, 57(1-2): 15-30. https://doi.org/10.3989/egeol.01571-2124

Ibouh, H.; Michard, A.; Hibti, M. & El Amari, K. (2011). Le cuivre des Couches Rouges de Tansrift (Atlas d'Azilal). Nouveaux Guides Géologiques et Miniers du Maroc, 9: 281-286.

Igmoullan, B.; Sadki, D.; Fedan & B.; Chellai EH (2001). Evolution géodynamique du Haut-Atlas de Midelt (Maroc) pendant le Jurassique: un exemple d'interaction entre la tectonique et l'eustatisme. Bulletin de l'Institut Scientifique 23: 47-54.

Inoue, A. & Utada, M. (1991). Smectite-to-chlorite transformation in thermally metamorphosed volcanoclastic rocks in the Kamikita area, northern Honshu, Japan. American Mineralogist, 76(3-4): 628-640.

Jacobshagen, S.; Altmüller, D.; Grolig, F. & Wagner, G. (1986). Calcium pools, calmodulin and light-regulated chloroplast movements in Mougeotia and Mesotaenium. In: Molecular and cellular aspects of calcium in plant development (Trewavas, A.J., Ed.). Springer, Boston, 201-209. https://doi.org/10.1007/978-1-4613-2177-4_25

Jacobshagen, V.; Brede, R.; Hauptmann, M.; Heinitz, W. & Zylka, R. (1988). Structure and post-Palaeozoic evolution of the central High Atlas. The atlas system of Morocco, 245-271. https://doi.org/10.1007/BFb0011596

Jacobshagen, V.; Brede, R.; Hauptmann, M.; Heinitz, W. & Zylka, R. (1988). Structure and post-Palaeozoic evolution of the central High Atlas. In: The Atlas System of Morocco (Jacobshagen, V.H., Ed.). Lecture Notes in Earth Sciences, 15. Springer, Berlin, Heidelberg. https://doi.org/10.1007/BFb0011596

Jenny, J. & Jossen, J.-A. (1982). Découverte d'empreintes de pas de Dinosauriens dans le Jurassique inférieur (Pliensbachien) du Haut Atlas central (Maroc). Comptes Rendus Academie Sciences Paris (II), 294: 223-226.

Jenny. J. & Le Marrec A. (1980): Mise en évidence d'une nappe à la limite méridionale du domaine hercynien dans la boutonnière d'Aït Tamlil (Haut Atlas central, Maroc). Eclogae Geologicae Helvetiae, 73/3: 681-696.

Jourda, J.P.; Saley, M.B.; Djagoua, E.V.; Kouame, K.J.; Biemi, J. & Razack, M. (2006). Utilisation des données ETM+ de Landsat et d'un SIG pour l'évaluation du potentiel en eau souterraine dans le milieu fissuré précambrien de la région de Korhogo (nord de la Côte d'Ivoire): approche par analyse multicritère et test de validation. Télédétection, 5(4): 339-357.

Kalinowski, A. & Oliver, S. (2004) Aster Mineral Index Processing Manual. Remote Sensing Application Geoscience, Australia, 36 pp.

Kouame, K.F. (1999). Hydrogéologie des aquifères discontinus de la région semimonta-gneuse de Man-Danané (Ouest de la Côte d'Ivoire). Apport des données des images satellitales et des méthodes statistiques et fractales à l'élaboration d'un système d'information hydrogéologique à référence spatiale. Thèse de 3e cycle, Université de Cocody (Abidjan-Côte d'Ivoire), 194 pp.

Lachaine, G. (1999). Structures géologiques et linéaments, Beauce (Québec): apport de la télédétection. MSc Memoire. Université de Sherbrooke, 105 pp.

Laville, E.; Fedan, B. & Pique, A. (1991). Jurassic penetrative deformation and cenozoic orogeny-2 stages of the development of the high atlas belt (morocco). Comptes Rendus de l'Academie des Sciences Serie II, 312(10): 1205-1211.

Laville, E.; Pique, A.; Amrhar, M. & Charroud, M. (2004). A restatement of the Mesozoic Atlasic rifting (Morocco). Journal of African Earth Sciences, 38(2): 145-153. https://doi.org/10.1016/j.jafrearsci.2003.12.003

Le Marrec, A. & Jenny, J. (1980). L'accident de Demnat, comportement synsedimentaire et tectonique d'un decrochement transversal du Haut-Atlas central (Maroc). Bulletin de la Société Géologique de France, 7(3): 421-427. https://doi.org/10.2113/gssgfbull.S7-XXII.3.421

Liu, L.; Ji, M.; Buchroithner, M.; Liu, L.; Ji, M.; Buchroithner, M.A (2018). Case Study of the Forced Invariance Approach for Soil Salinity Estimation in Vegetation-Covered Terrain Using Airborne Hyperspectral Imagery. ISPRS International Journal of Geo-Information, 7: 48. https://doi.org/10.3390/ijgi7020048

Loughlin, W.P. (1991). Principal Component Analysis for Alteration Mapping. Photo-grammetric Engineering and Remote Sensing, 57: 1163-1169.

Mattauer, M.; Tapponnier, P. & Proust, F. (1977). Les mecanismes de formation des chaines intracontinentales; l'exemple des chaines atlasiques du Maroc. Bulletin de la Société géologique de France, 7(3): 521-526. https://doi.org/10.2113/gssgfbull.S7-XIX.3.521

Michard A. (1976). Éléments de géologie marocaine. Notes et Mémoires du Service Géologique de Maroc, 252: 1-408.

Michard, A.; Ibouh, H. & Charrière, A. (2011). Syncline-topped anticlinal ridges from the High Atlas: a Moroccan conundrum, and inspiring structures from the Syrian Arc, Israel. Terra Nova, 23(5): 314-323. https://doi.org/10.1111/j.1365-3121.2011.01016.x

Mouguina, E.M. (1992). Minéralisations polyphasées de couverture (Zn, Pb, Cu, Fe, As) liées au magmatisme d'un rift avorté au Jurassique. Doct.Spéc., Université de Tunis, 186 pp.

Mouguina, E.M. & Daoudi, L. (2008). Minéralisation Pb-Zn du type MVT de la région d'Ali ou Daoud (Haut Atlas Central, Maroc): caractérisations du gîte et relations avec les cortèges de minéraux argileux. Estudios Geológicos, 64(2): 135-150. https://doi.org/10.3989/egeol.08642.038

Mouguina, E.M. (2004). Les minéralisations polymétalliques (Zn-Pb, Cu, Co, Ni) du Juras-sique du Haut Atlas central (Maroc): Contexte géodynamique, typologies et modèles génétiques. PhD Thesis, Université Cadi-Ayyad, Marrakech, 320 pp.

Mouguina, E.M.; Bouabdelli, M. & Tlig, S. (1999). Le gisement à Pb-Zn de Tazoult (Haut-Atlas central, Maroc): caractères géologiques, minéralogiques et géochimiques. Modèle tectonique de mise en place. Chronique de la recherche minière, 536-537: 151-169.

Muhammad, M.M. & Awdal, A.H. (2012). Automatic mapping of lineaments using shaded relief images derived from digital elevation model (DEM) in Erbil-Kurdistan, northeast Iraq. Advances in Natural and Applied Sciences, 6(2): 138-147.

Nouayti, N.; Khattach, D. & Hilali, M. (2017). Cartographie des zones potentielles pour le stockage des eaux souterraines dans le haut bassin du Ziz (Maroc): Apport de la télédétection et du système d'information géographique. Bulletin de l'Institut Scientifique, Section Sciences de la Terre, 39(45-57): 1-13.

Othman, A.; Gloaguen, R (2014). Improving Lithological Mapping by SVM Classification of Spectral and Morphological Features: The Discovery of a New Chromite Body in the Mawat Ophiolite Complex (Kurdistan, NE Iraq). Remote Sensing, 6: 6867-6896. https://doi.org/10.3390/rs6086867

Othman, A.A.; Gloaguen, R. (2017) Integration of spectral, spatial and morphometric data into lithological mapping: A comparison of di_erent Machine Learning Algorithms in the Kurdistan Region, NE Iraq. Journal of Asian Earth Sciences, 146: 90-102. https://doi.org/10.1016/j.jseaes.2017.05.005

Ourhzif, Z.; Algouti, A. & Hadach, F. (2019). Lithological mapping using Landsat 8 OLI and Aster multispectral data in Imini-Ounilla district South High Atlas of Marrakech. International Archives of the Photogrammetry, Remote Sensing & Spatial Information Sciences, XLII-2/W13: 1255–1262. https://doi.org/10.5194/isprs-archives-XLII-2-W13-1255-2019

Piqué, A. (1979). Evolution structurale d'un segment de la chaîne hercynienne. La Meseta marocaine nord-occidentale. PhD Thesis, Université Louis Pasteur, Strasbourg, 243 pp.

Piqué, A.; Bossière, G.; Bouillin, J.P.; Chalouan, A. & Hoepffner, C. (1993). Southern margin of the Variscan belt: the north-western Gondwana mobile zone (eastern Morocco and northern Algeria). Geologische Rundschau, 82(3): 432-439. https://doi.org/10.1007/BF00212407

Pour, A.B. & Hashim, M. (2014). ASTER, ALI and hyperion sensors data for lithological mapping and ore minerals exploration. SpringerPlus, 3: 130. https://doi.org/10.1186/2193-1801-3-130

Pournamdari M.; Hashim M. & Beiranvand Pour, A. (2014). Spectral transformation of ASTER and Landsat TM bands for lithological mapping of Soghan ophiolite complex, south Iran, Advances in Space Research, 54(4): 694-709. https://doi.org/10.1016/j.asr.2014.04.022

Qaid, A.M. & Basavarajappa, H.T. (2008). Application of optimum index factor technique to Landsat-7 data for geological mapping of north east of Hajjah, Yemen. American-Eurasian Journal of Scientific Research, 3(1): 84-91.

Ranjbar H.M. Honarmand, Z. & Moezifar (2004). Application of the Crosta technique for porphyry copper alteration mapping, using ETM+ data in the southern part of the Iranian volcanic sedimentary belt, Journal of Asian Earth Sciences, 24(2): 237-243. https://doi.org/10.1016/j.jseaes.2003.11.001

Rokos, D.; Argialas, D.; Mavrantza, R.; St-Seymour, K.; Vamvoukakis, C.; Kouli, M.; Lamera, S.; Paraskevas, H.; Karfakis, I. & Denes, G. (2000). Structural analysis for gold mineralization using remote sensing and geochemical techniques in a GIS environment: island of Lesvos, Hellas. Natural Resources Research, 9(4): 277-293. https://doi.org/10.1023/A:1011505326148

Rowan, L.C. & Mars, J.C. (2003). Lithologic mapping in the Mountain Pass, California area using advanced spaceborne thermal emission and reflection radiometer (ASTER) data. Remote sensing of Environment, 84(3): 350-366. https://doi.org/10.1016/S0034-4257(02)00127-X

Rowan, L.C.; Hook, S.J.; Abrams, M.J. & Mars, J.C. (2003). Mapping hydrothermally altered rocks at Cuprite, Nevada, using the Advanced Spaceborne Thermal Emission and Reflection Radiometer (ASTER), a new satellite-imaging sys-tem. Economic Geology, 98(5): 1019-1027. https://doi.org/10.2113/gsecongeo.98.5.1019

Saadi, N.M.; Abdel Zaher, M.; El-Baz, F. & Watanabe, K (2011). Integrated remote sensing data utilization for investigating structural and tectonic history of the Ghadames Basin, Libya. International Journal of Applied Earth Observation and Geo-information, 13: 778-791. https://doi.org/10.1016/j.jag.2011.05.016

Stets, J. & Wurster, P. (1982). Atlas and Atlantic-structural relations. In: Geology of the Northwest African continental margin (Rad, U.; Hinz, K.; Sarnthein, M. & Seibold, E., Eds.), Springer, Berlin, 69-85. https://doi.org/10.1007/978-3-642-68409-8_5

Tabeliouna M.; Kaddour H.; Zeroual I. (2016). Cartographie Par Imagerie Satellitale et Discrimination Lithologique du Complexe Magmatique d'anna (Eglab, Dorsale Reguibat, Sud-Ouest Algerien). Abstracts of the 3rd International Conference of GIS Users, Oujda, Maroc, 3: 263-268.

Tangestani, M.H.; Mazhari, N.; Agar, B. & Moore, F. (2008). Evaluating Advanced Spaceborne Thermal Emission and Reflection Radiometer (ASTER) data for altera-tion zone enhancement in a semi-arid area, northern Shahr-e-Babak, SE Iran. International Journal of Remote Sensing, 29(10): 2833-2850. https://doi.org/10.1080/01431160701422239

Teixell, A.; Barnolas, A.; Rosales I & Arboleya ML. (2017). Structural and facies architec-ture of a diapir-related carbonate minibasin (lower and middle Jurassic, High Atlas, Morocco). Marine and Petroleum Geology, 81: 334-360. https://doi.org/10.1016/j.marpetgeo.2017.01.003

Van der Meer, F.; Hecker, C.; van Ruitenbeek, F.; Van der Werff, H.; De Wijkerslooth, C. & Wechsler, C. (2014). Geologic remote sensing for geothermal exploration: A review. International Journal of Applied Earth Observation and Geoinformation, 33: 255-269. https://doi.org/10.1016/j.jag.2014.05.007

Van Der Werff, H.M.A. & Van Der Meer, F.D. (2016). Sentinel 2A MSI and Landsat 8 OLI provide data continuity for geological remote sensing. Remote Sensing, 8: 883. https://doi.org/10.3390/rs8110883

Varas, O.T.P. (2006). Lineament extraction from digital terrain models: case study san antonio del sur area, south-eastern Cuba. MSc Thesis, International Institute for Geo-information Science and Earth Observation, Enshede, 81 pp.

Youan Ta, M.; Lasm, T.; Jourda, J.P.; Kouame, K.F. & Razack, M. (2008). Cartographie des accidents géologiques par imagerie satellitaire Landsat-7 ETM+ et analyse des réseaux de fractures du socle précambrien de la région de Bondoukou (nord-est de la Côte d'Ivoire). Télédétection, 2: 34-42.

Yu, L.; porwal, a.; holden, e.-j.; dentith, m.c (2012). Towards automatic lithological classification from remote sensing data using support vector machines. Computers & Geosciences, 45: 229-239. https://doi.org/10.1016/j.cageo.2011.11.019